Light Generation, Amplification, and Wavelength Conversion via Stimulated Raman Scattering in Silicon Microstructures

Bahram Jalali, Ricardo Claps,
Dimitri Dimitropoulos, and Varun Raghunathan

Department of Electrical Engineering, University of California
Los Angeles, CA 90095-1594, USA
jalali@ucla.edu

Abstract. This chapter is organized in two parts. In part one, we present the theory of Spontaneous and Stimulated Raman Scattering (SRS), as well as that of Coherent Anti Stokes Raman Scattering (CARS) in silicon. The treatment of these phenomena in silicon is more complex than that in silica fiber, due to crystal symmetry considerations. We show that, because of the intrinsically large Raman coefficient in silicon, and the tight optical confinement in silicon-on-SiO$_2$ waveguides, both amplification and wavelength conversion can be achieved in waveguides with millimeter scale lengths. In part two, we review our recent demonstration of spontaneous Raman emission, optical gain, and wavelength conversion in silicon waveguides. The chapter concludes by discussing practical issues and methods for realizing commercially viable devices.

1 Introduction

Silicon is the ideal platform for integrated optics and optoelectronics. Driven by the electronic IC industry, the quality of commercial silicon wafers continues to improve while the cost continues to decrease. This, along with compatibility with silicon IC manufacturing and silicon MEMS technology, is fuelling interest in silicon photonics [1]. Compared to other integrated optics platforms, a distinguishing property of silicon is the tight optical confinement made possible by the large index mismatch between the silicon and SiO$_2$. This renders silicon ideal for realization of photonic band structures as it minimizes radiation into the substrate even when extreme index modulation is performed. While a myriad of high performance passive devices has been realized [1], creation of active devices has been an elusive goal. In particular, the near-absence of nonlinear optical properties caused by the symmetric crystal structure, and the lack of efficient optical transitions due to the indirect band structure, have contributed to the premature perception of silicon being useful only as an optically passive material.

The need for active devices has stimulated significant amount of research, mostly in light generation in silicon. While the progress was slow in the early

years, several breakthroughs have been made in the last three years. Various approaches that have been investigated for light generation consist of: 1. silicon nanocrystals, 2. Erbium doped silicon-rich oxide, 3. surface-textured bulk silicon, and 4. Si/SiGe quantum cascade structures. Silicon nanocrystals have received the most attention, and indications of stimulated emission have been observed in these structures [2, 3, 4, 5, 6, 7, 8, 9]. The nanocrystal approach, in which silicon nano-particles are formed within an SiO_2 film, has been motivated by earlier observation of light emission in porous silicon [10]. Porous silicon suffers from stability due to the high reactivity of exposed silicon surfaces, rendering it non-ideal for device applications. This problem is mitigated when the nanocrystals reside within the oxide layer. The structures are formed by high temperature anneal of a nonstochiometric silicon-rich oxide. The latter can be formed by 1. implantation of silicon into SiO_2, 2. Plasma Enhanced Deposition (PECVD), or 3. sputter deposition. The latter two approaches may be preferred over implantation since they produce a more uniform distribution of silicon within the oxide and hence, a narrower size distribution of nanocrystals.

The main limitation of silicon nanocrystals is that the emission occurs at wavelengths below 1000 nm, away from the important bands for telecommunication applications (1300 nm and 1550 nm). This problem has been mitigated by incorporating rare-earth dopants into the system [10,11]. The emission wavelength can be engineered by choosing the particular dopants (Er, Yb, Pr, etc.) [12]. Additionally, structures can be electrically pumped by impact ionization, caused by hot electrons injection, realized in a Metal Oxide Semiconductor (MOS) diode. Using these two approaches, silicon LEDs with $\sim 10\%$ efficiencies and output powers approaching 100 µW have recently been demonstrated [12,13]. These devices would be competitive with III–V LEDs once reliability issues are resolved.

By using high purity silicon, minimizing recombination at surfaces and electrical contacts, and texturing the surface to enhance the escape of photons, LEDs with efficiencies of 1%–10% have been demonstrated [14]. The measured spontaneous emission is due to the band-to-band transitions in bulk silicon and is centered at approximately 1100 nm wavelength. The main limitation of this approach is its slow modulation speed, limited by the long (ms) lifetime in high purity silicon. Also, stimulated emission is yet to be demonstrated.

Another approach to light generation in silicon is through intra-band transitions in Si/SiGe quantum cascade systems [15,16,17]. The approach is similar to celebrated quantum cascade lasers in III–V semiconductors capable of producing coherent radiation in the mid-IR spectrum [18]. In silicon, the concept is implemented with holes, since most of the band offset occurs in the valence band in strained layer Si/SiGe epitaxial layers. The strain caused by the lattice mismatch between Si and SiGe limits the number of layers that can be grown defect free. This, along with a high effective mass of holes

makes realization of silicon quantum cascade devices more challenging than their III–V counterparts. Nonetheless, excellent progress is being made and electroluminescence from such devices has been demonstrated [17, 19].

At UCLA, we have taken an entirely different approach to achieving optical functionality in silicon, namely through Raman scattering [20, 21, 22, 23, 24, 25, 26, 27, 28, 29, 30, 31]. The Raman effect is successfully exploited in fiber amplifiers and lasers; however, several kilometers of fiber are required to create a useful device. Fortunately, the gain coefficient for Stimulated Raman Scattering (SRS) is approximately 10^4 times higher in silicon than in silica. Additionally, SOI waveguides can confine the optical field to an area that is approximately 100 times smaller than the modal area in a standard single mode optical fiber. The combination of these properties will make SRS observable over the millimeter-scale interaction lengths encountered in an integrated optic device. A desirable feature of Raman scattering is that light generation and amplification can be achieved at any wavelength (as long as the corresponding pump laser wavelength is available). Further, it does not require special impurities; therefore, the resulting devices are truly compatible with silicon manufacturing.

In addition to light generation and amplification, we have shown that the Raman effect can also perform wavelength conversion [28, 29, 30, 31]. The conversion is achieved by the Stimulated Raman Scattering (SRS) contribution to the third order nonlinear susceptibility. Stokes to Anti-Stokes coupling occurs through coherent interaction of the two waves with a high intensity pump. Wavelength conversion is of paramount importance in optical networks because it enables optical packet switching, a milestone in the realization of all-optical networks. A key issue is to realize high conversion efficiencies. Since the efficiency in typical waveguides is limited by phase mismatch, the crucial problem is how to engineer the Group Velocity Dispersion (GVD) inside the waveguide in order to attain phase matching. The last section in this chapter describes how this can be achieved using birefringence to compensate for material dispersion in silicon waveguides.

2   Theory of Raman Scattering in Silicon

2.1   Spontaneous Raman Emission

Raman scattering in silicon was the subject of extensive research in the early 1970s as a means to study optical phonons in the material [32]. Measurements were performed on bulk silicon and at visible wavelengths. As expected, first-order Raman scattering in silicon is due to the scattering of light by the threefold degenerate zone-center optical phonons in the crystal. It corresponds to the largest feature observed in the Raman spectrum of silicon, shown in Fig. 1, where second-order Raman scattering modes are also shown. These second order modes are nearly 2 orders of magnitude weaker than the fundamental mode and will not be considered any further in the
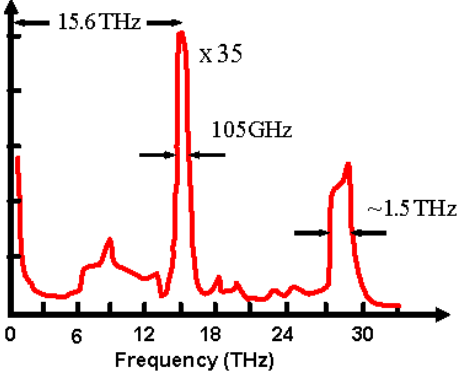
Fig. 1. Raman Spectrum of Silicon (from [32])

present manuscript. Throughout this chapter, the first-order Raman mode will be referred to as the "Stokes" scattered field, whereas the incident field that generates the process will be referred to as the "pump" field. The Stokes frequency, ω_s, is ~ 15.6 THz down-shifted from the pump frequency, ω_p, this shift corresponds to the frequency of the zone center optical phonon in silicon, from now on denoted as Ω. The FWHM of the spectra is ~ 105 GHz and gives rise to a response time of ~ 10 ps for the Raman process in silicon. The amount of Raman radiation obtained from a given material is determined by the spontaneous scattering efficiency, S $(\mathrm{cm}^{-1} \cdot \mathrm{sr}^{-1})$, which relates the pump intensity, I_p $(\mathrm{W/cm}^2)$ to the total Stokes–Raman power, P_R (W), measured over a solid angle, Φ (sr), scattered from a volume, V, of the material,

$$P_R = (\Phi \times V) \times S \times I_P. \tag{1}$$

A more detailed analysis of the Raman scattering process needs to take into account the crystal symmetry of silicon. Furthermore, it is necessary to pave the way for introducing nonlinear effects in the picture (which will be detailed in the following section). The most convenient way to do this, is through the induced-polarization vector, $\boldsymbol{P}(\omega_s)$, and the pump electric field, $\boldsymbol{E}(\omega_p)$, responsible for the Stokes radiation associated with the phonon displacement, $\boldsymbol{Q}$. The induced polarization is related to the incident electric field as [33, 34]:

$$P_i(\omega_s) = R_{ijk} Q_k^* \times E_j(\omega_p). \tag{2}$$

Equation (2) defines the Raman tensor, $\boldsymbol{R}$ Its components, R_{ijk}, are proportional to $\partial a_{ij}/\partial Q_k$, where a is the polarizability of the material. The term, Q_k, in (2) is the kth component of the phonon mode, $\boldsymbol{Q}$, and ω_p and ω_s are the pump and Stokes frequencies, respectively. In the linear domain, where the pump power levels are below a threshold value, the tensor $\boldsymbol{R}$ is independent of the pump electric field, and can be defined in terms of the

scattering efficiency, S, as follows [35]

$$S = S_0 \sum_{n=1,2,3} |\hat{e}_s R_n \hat{e}_p|^2 . \tag{3}$$

The vectors $\hat{e}_p$ and $\hat{e}_s$ denote the polarization of the pump and Stokes electromagnetic fields. S_0 is an intrinsic microscopic property of silicon and has the same dimensions as S. It contains specific information about the derivatives of the polarizability in silicon, and the absolute amplitude of the displacement of the zone-center optical phonons in the crystal. Another parameter that is usually seen in the literature is the linear Raman susceptibility, χ_R, which is related to S_0 through the following expression [33],

$$S_0 = \frac{k_S^4}{32\pi^2 n} V \chi_R^2 , \tag{4}$$

where k_s is the wavevector of the Stokes wave, $k_s = 2\pi n_s/\lambda_S$, n_s is the index of refraction, and V is the same as in (1). Given the scattering efficiency for a particular wavelength, S_0 can be calculated for other wavelengths by taking into account the λs^{-4} dependence given by (4). The value of S_0 at $\sim 1550\,\mathrm{nm}$ is estimated to be $8.4 \times 10^{-7}\,\mathrm{cm}^{-1} \cdot \mathrm{sr}^{-1}$ [20].

In a coordinate system oriented along the crystallographic axes of silicon, the Raman tensor components are given as [23]:

$$\overleftrightarrow{R}_1 = \begin{bmatrix} 0 & 1 & 0 \\ 1 & 0 & 0 \\ 0 & 0 & 0 \end{bmatrix}, \quad \overleftrightarrow{R}_2 = \begin{bmatrix} 0 & 0 & 1 \\ 0 & 0 & 0 \\ 1 & 0 & 0 \end{bmatrix}, \quad \overleftrightarrow{R}_3 = \begin{bmatrix} 0 & 0 & 0 \\ 0 & 0 & 1 \\ 0 & 1 & 0 \end{bmatrix} . \tag{5}$$

Table 1 shows the relative spontaneous Raman intensities obtained for different scattering configurations in silicon. The table is obtained by using the tensor components in (5) into (3) and solving for the absolute scattering intensity. In the table, the vectors $\hat{k}_p$ and $\hat{k}_s$ denote the pump and Stokes field propagation, respectively, and for the case of forward scattering are identical.

Table 1. Spontaneous Scattering efficiency for various wavevector and polarization directions of Pump and Stokes fields

$\hat{k}_p$ & $\hat{k}_s$	$\hat{e}_p$	$\hat{e}_s$	Relative efficiency
$[1\bar{1}0]$	$[110]$	$[110]$	S_0
$[1\bar{1}0]$	$[110]$	$[001]$	S_0
$[11\bar{2}]$	$[111]$	$[111]$	$4S_0/3$
$[111]$	$[1\bar{1}0]$	$[11\bar{2}]$	$2S_0/3$
$[111]$	$[11\bar{2}]$	$[11\bar{2}]$	S_0
$[0\bar{1}1]$	$[011]$	$[100]$	S_0
$[0\bar{1}1]$	$[011]$	$[011]$	S_0
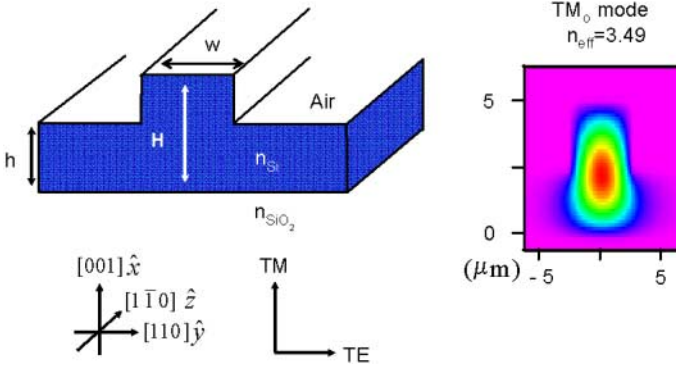
Fig. 2. SOI waveguides used. The *coordinate axes* are labeled in the usual crystallographic notation. The (x, y, z) labels appear as they will be used throughout the text. The resulting TM_0 mode ($\lambda = 1.54\,\mu m$) from a BPM calculation is depicted to the *right*, for the case $H = w = 5.0\,\mu m$, $h = 2.2\,\mu m$. The effective index of refraction is calculated assuming $n = 3.5$ for bulk silicon

From Table 1, it is seen that the configuration oriented along the $[1\bar{1}0]$ direction has the property that the scattering intensity is polarization independent, with the pump field oriented along the $[110]$ direction. This, together with the favorable cleaving properties of silicon in this orientation, makes the afore-mentioned configuration highly convenient if one is thinking in terms of a polarization-independent device. For this reason, the theoretical and experimental work presented here is based on rib waveguides fabricated parallel to the $[1\bar{1}0]$ direction on a $[001]$ silicon surface. The cross-section of the rib structure and a typical mode profile associated with it, are shown in Fig. 2, together with a convenient selection of a coordinate axes system (x, y, z) that will be used for the remainder of this chapter.

2.2   Stimulated Raman Scattering

When the intensity of the pump field inside the material surpasses certain threshold value, the linear regime in which (3) applies is no longer valid, and the process of Stimulated Raman Scattering (SRS) takes place. The nonlinear effect concerns the electric field dependence of the induced polarization. This dependence can be obtained by solving for the phonon displacement, $\boldsymbol{Q}$. The equation of motion for $\boldsymbol{Q}$ is governed by the differential equation for a forced-harmonic oscillator with damping coefficient, Γ, and resonance frequency, Ω [34]:

$$\frac{\mathrm{d}^2 Q_k}{\mathrm{d}t^2} - 2\Gamma \frac{\mathrm{d}Q_k}{\mathrm{d}t} + \Omega^2 Q_k = R_{kmn} E_m(-\omega_\mathrm{p}) E_n(\omega_\mathrm{s}) , \tag{6}$$

where use has been made of the fact that the force on the Q_k phonon component goes as $F_{Q_k} = -\partial\varepsilon/\partial Q_k$, with $\varepsilon = -\boldsymbol{P} \times \boldsymbol{E}$, and $\boldsymbol{P}$ as given by (2).

Equation (6) is solved for Q in terms of the pump and Stokes electric fields. It is customary to define the nonlinear susceptibility, χ_{ijmn}^{R}, by the following relation:

$$P_i^{NL}(\omega_s) = \varepsilon_0 \chi_{ijmn}^{R} E_j(\omega_p) E_m(-\omega_p) E_n(\omega_s) \,. \tag{7}$$

By introducing the solution for (6) into (2), and comparing with the definition given in (7), we arrive at the following expression for χ_{ijmn}^{R}

$$\chi_{ijmn}^{R} = \frac{1}{\varepsilon_0} \frac{R_{ijk} R_{kmn}}{(\Omega^2 - (\omega_p - \omega_s)^2 - 2i\Gamma(\omega_p - \omega_s))} \,, \tag{8}$$

The pump and signal frequencies, ω_p and ω_s, respectively, need not satisfy the 'Raman-resonance' condition: $\omega_p - \omega_s = \Omega$. It will be demonstrated below that the nonlinear optical constants for bulk silicon can be used to accurately describe the rib-SOI waveguides, shown in Fig. 2 with negligible correction factors for Raman-induced cross-polarization effects. Equation (8) will be useful in the next section; there, a full vectorial treatment of the electric fields in the waveguide will be necessary to carry out Coupled-Mode calculations of the SRS effect in SOI waveguides. For the moment, we will proceed with an approach that considers bulk propagation. In this regime, the gain coefficient, g_R, defined through the relation, $dP_R/dz = g_R P_R I_p$ (cf 1), is obtained from the spontaneous scattering efficiency, S, as [35]:

$$g_R = \frac{8\pi c^2 \omega_p}{\hbar \omega_s^4 n^2(\omega_s)(N+1)\Delta\omega} S \,, \tag{9}$$

The factor N is the Bose occupation number (0.1 at room temperature), and $\Delta\omega$ is the FWHM of the spontaneous Raman spectrum. The relation between g_R and χ_{ijmn}^{R} will be made explicit below. Substituting the appropriate values, the gain coefficient is obtained as 0.076 cm/MW. When compared to silica (0.93×10^{-5} cm/MW) [36,37], the Raman gain in silicon is approximately 10^4 times larger! Such a large difference has its origin in the linewidth of the Raman spectrum being much narrower in crystalline silicon compared to the amorphous fiber. The relation between g_R and χ_{ijmn}^{R} can be obtained from Maxwell's equations and (7) as [27]

$$\chi_{2222}^{R}(\omega_p - \omega_s = \Omega) = \frac{i}{(\mu_0/\varepsilon_0)^{1/2}} \frac{2ncg_R}{\omega_s} = 11.2 \times 10^{-14} i \, \frac{cm^2}{V^2} \,.$$

Following the same derivation for the total Raman amplification in optical fibers [21], the amplified Stokes signal power after a length, L, in the rib waveguide, with an initial input stokes power of $P_R(0)$ is given as [21]:

$$P_R(L) = P_R(0) \exp\left[-\gamma L + \frac{g_R I_P(0)}{\gamma}(1 - \exp(-\gamma L))\right] \,, \tag{10}$$
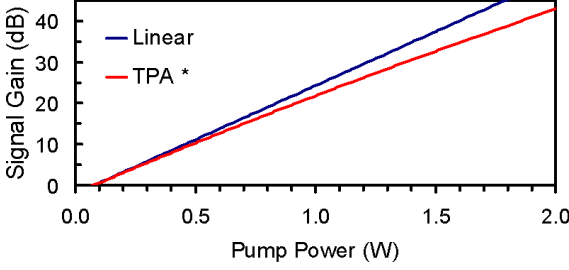
Fig. 3. Stimulated Raman gain as a function of the pump power with no other nonlinear contribution and with two-photon-absorption (TPA). $L = 1.9\,\mathrm{cm}$, $\gamma = 1\,\mathrm{dB/cm}$, $g_\mathrm{R} = 0.076\,\mathrm{cm/MW}$, $a = 2\,\mathrm{\mu m^2}$, $P_\mathrm{R} = 1\,\mathrm{\mu W}$

where γ is the propagation loss (cm^{-1}), $I_\mathrm{p}(0) = P_\mathrm{p}(0)/A$ is the input pump intensity, and A is the modal overlap between the propagating $\mathrm{TE_0}$ and $\mathrm{TM_0}$ waveguide modes. The plot of the net Stokes gain as a function of the pump power for a waveguide of length, $L = 1.9\,\mathrm{cm}$, is shown in Fig. 3. The plot shows that more than $10\,\mathrm{dB}$ gain can be obtained with a pump power of less than $50\,\mathrm{mW}$. Moreover, the threshold power, which is defined as the pump power required to achieving transparency, is relatively small in comparison to fibers, because of the tight confinement of the optical fields in the rib structure. The use of low-loss waveguides with efficient coupling schemes, and antireflection coated facets, can reduce the threshold power even further. The pump is assumed to be a monochromatic source. The finite linewidth of the pump laser will result in a lower gain than what is predicted in Fig. 3. The effect of the pump linewidth is discussed in Sect. 3.2.1. At high enough pump powers, two photon absorption (TPA) may contribute significantly towards pump depletion. Including TPA in (10) involves reduction of the pump power with distance, as given below [20]:

$$P_\mathrm{p}(z) = \frac{P_\mathrm{p}(0)e^{-\gamma z}}{(1 + B\,z\,I_\mathrm{p}(0))}, \tag{11}$$

where B $(\mathrm{cm/W})$ is the TPA coefficient for silicon. The effect of TPA is a negligible reduction in gain, as shown in Fig. 3.

It is clear that for amplification levels of up to $10\,\mathrm{dB}$, the gain reduction produced by TPA is below 10%. The value of B used to plot Fig. 3 was obtained from experiments described in Sect. 3.2.2. Another nonlinear effect in silicon that may affect the Raman gain coefficient is Coherent Anti-Stokes Raman Scattering (CARS). As will be described in Sect. 3.3, this effect can actually be exploited in performing wavelength conversion when a phase matching condition is satisfied. The results presented up to this point start from the basis that there is no coupling between the $\mathrm{TE_0}$ and $\mathrm{TM_0}$ modes of propagation along the waveguide. This simplifies the analysis and eventually leads to (10). In single-mode silica fibers, this assumption is justified because

the Raman signal has the same polarization as the pump signal. As we have seen (cf Table 1) this is not the case for crystalline silicon, where the pump and Stokes fields have crossed polarization, and therefore the fields couple to different modes in the waveguide. In the next section, we will use a detailed Coupled-Mode-Calculation theory (CMC) to investigate the issue of Raman-induced cross-coupling between TE_0 and TM_0 field modes, and demonstrate the validity of (10) and the results derived from it (Fig. 3).

2.3   Coupled-Mode Theory Analysis of Raman Scattering

In the rib SOI waveguide, with the pump field being launched in the TE_0 mode and the Stokes field assumed to be in both TE_0 and TM_0 modes, these fields can be represented mathematically as follows:

$$\boldsymbol{E}(\omega_\text{s}) = \sum_{\mu=1,2} A_{s,\mu} \in_\mu(\omega_\text{s}, x, y) e^{i\beta_\mu z} ,$$
$$\boldsymbol{E}(\omega_\text{p}) = A_{p,1} \in_1(\omega_\text{p}, x, y) e^{i\beta_1 z} ,$$

(12)

where μ denotes the polarization of the field (1 for TE_0, and 2 for TM_0), $A_{s,1} = \sqrt{a P_\text{s}}$, $A_{s,2} = \sqrt{(1-a)P_\text{s}}$, a is the fractional power in the TE_0 polarization, $A_{p,1} = \sqrt{P_\text{p}}$, P_p denotes the coupled pump power (W), $\in$ denotes the normalized modal profile, and β_μ (cm^{-1}) is given by $\beta_\mu = 2\pi\, n_\mu / \lambda_\mu$, as usual ($n_\mu$ is the effective index of refraction of the mode in question). The coupled mode equations relating the Stokes field in TE_0 and TM_0 polarizations, with no pump depletion, are given as follows [27, 34]:

$$\frac{\mathrm{d}A_{s,1}}{\mathrm{d}z} = i\kappa_{11} P_\text{p} A_{s,1} + i\kappa_{12} P_\text{p} A_{s,2} \exp(i(\beta_2 - \beta_1)z) ,$$

(13a)

$$\frac{\mathrm{d}A_{s,2}}{\mathrm{d}z} = i\kappa_{22} P_\text{p} A_{s,2} + i\kappa_{21} P_\text{p} A_{s,1} \exp(-i(\beta_2 - \beta_1)z) .$$

(13b)

The coupling coefficients $\kappa_{\mu\mu'}$ are given by:

$$\kappa_{\mu\mu'} = -i \sum_{i,j,m,n=1,2,3} \frac{2g_\text{R}}{Z^2} \xi_{ijmn}$$
$$\times \iint \in_\mu^{*i}(\omega_\text{s}) \in_1^j(\omega_\text{p}) \in_1^{*m}(\omega_\text{p}) \in_{\mu'}^n(\omega_\text{s}) \mathrm{d}x \mathrm{d}y , \quad (14)$$

where $Z = Z_0/n_{Si}$ is the impedance in the waveguide ($Z_0 = (\mu_0/\varepsilon_0)^{1/2} = 377\,\Omega$ [43]), $\xi_{ijmn} = \chi_{ijmn}^R/\chi_{1111}^R$ and $\in_\mu^i$ is the mode profile of the ith component of the μ polarization-mode vector. In the case of weak coupling the gain, G (dB/cm), will be given by,

$$G_{\text{TE(TM)}} = 4.34 \times 2 \left|\kappa_{11(22)}\right| P_\text{p} .$$

(15)

For the spontaneous Raman Effect, the coupled-mode equations as mentioned above are modified into the following form:

$$\frac{\mathrm{d}A_{s,\mu,\nu}}{\mathrm{d}z} = i\bar{\kappa}_{\mu\nu} A_{p,1} .$$

(16)

The index ν refers to the optical phonon component. The coupling coefficients in this case are

$$\bar{\kappa}_{\mu,\nu} = \omega_s \varepsilon_0 \chi_R \iint \in_{\mu}^*(\omega_s) \boldsymbol{R}_\nu \in_1(\omega_p) \mathrm{d}x \mathrm{d}y \,. \tag{17}$$

The scattering efficiency for a Stokes mode μ, S_μ, is defined as

$$S_\mu = \frac{|A_{s,\mu}|^2}{|A_{p,1}|^2 l} = l \left(|\bar{\kappa}_{\mu,1}|^2 + |\bar{\kappa}_{\mu,2}|^2 + |\bar{\kappa}_{\mu,3}|^2 \right) \,. \tag{18}$$

Comparing (3), (17) and (18), S_μ can be rewritten as:

$$S_\mu = S_0 \frac{32\pi^2}{k_0^4} \omega^2 \varepsilon_0^2 \frac{\sum\limits_{\lambda=1,2,3} \left| \iint (\varepsilon_\mu(\omega_s))^* \times \vec{R}_\lambda \times \varepsilon_1(\omega_p) \mathrm{d}x \mathrm{d}y \right|^2}{A_{\mathrm{eff}}} \,, \tag{19}$$

with the scattering volume, $V = A_{\mathrm{eff}} l$, and A_{eff} taken as the effective area of the TE$_0$ pump mode:

$$A_{\mathrm{eff}} = \frac{\left(\iint |\varepsilon_1(\omega_p)|^2 \, \mathrm{d}x \mathrm{d}y \right)^2}{\iint |\varepsilon_1(\omega_p)|^4 \, \mathrm{d}x \mathrm{d}y} \,. \tag{20}$$

Table 2 lists the coupling coefficients and the modal scattering efficiency, S_μ, for varying rib widths, with the rib height and slab height varied proportional to the widths [27]. The mode profiles that were used in computing the coefficients in (14), (19) and (20) were evaluated using a finite-difference time domain method [38]. Now it is possible to define an effective area, A_R^{eff}, by relating the effective gain obtained from (15), to the bulk Raman gain, g_R, as expressed in (9) above. This relation can be written as

$$2\kappa_{11(22)} P_P = g_R I_p = g_R P_P / A_R^{\mathrm{eff}} \,. \tag{21}$$

Using (21), it is seen that the value of A_R^{eff} decreases linearly as the waveguide dimensions are reduced, whereas the spontaneous efficiency (19) and the gain coefficient (15) are found to increase, as expected. The modal spontaneous efficiencies are larger for TE$_0$ than for TM$_0$ modes, but the gain coefficients follow the opposite trend. Though this contradicts the Einstein relation between spontaneous efficiency and gain, this trend is in fact real. The validity of Einstein's relation is limited to electric fields with spatial homogeneity and isotropic energy density [39], and as the waveguide dimensions are reduced, this assumption is no longer valid and the effect mentioned above is observed. It is also clear that the inter-modal coupling coefficients are less

than two orders of magnitude smaller than the self coupling coefficients. This implies that the two Stokes modes propagate independent of each other, confirming the validity of the approach leading to (10). Furthermore, the CMC analysis proves that simultaneous amplification of TE_0/TM_0 Stokes modes is possible through polarization multiplexing of the signals.

Table 2. Effective area, coupling coefficients and spontaneous efficiency for a rib waveguide with $w/h = 2/1.4$ and $w/H = 2/2.15$

w	A_R^{eff}	A_R^{eff}	κ_{11}	κ_{22}	κ_{12}	S_{TE}	S_{TM}
	TE	TM	TE	TM	(10^{-3})		
(μm)	(μm^2)	(μm^2)	$(cmW)^{-1}$	$(cmW)^{-1}$	$(cmW)^{-1}$	$(10^{-9}\,cm^{-1})$	$(10^{-9}\,cm^{-1})$
4	16.2	15.3	$-j0.215$	$-j0.23$	$-0.32 - j0.58$	19.6	19.2
3	8.9	8.25	$-j0.39$	$-j0.42$	$-2.5 + j1.36$	35.8	35.2
2	4.3	3.9	$-j0.82$	$-j0.89$	$-11.9 + j13.3$	69.2	67.0
1.2	1.6	1.4	$-j2.16$	$-j2.45$	$-284 + j89.7$	192	183
0.8	1.1	0.9	$-j3.1$	$-j3.88$	$212 - j69.5$	271.2	222.0
0.4	0.42	0.36	$-j8.28$	$-j9.7$	$-58.9 - j18$	787.0	540.0

2.4   Coherent Anti-Stokes Raman Scattering (CARS) in Silicon

In the previous analysis of the Raman process in silicon, no mention was made of the anti-Stokes field (also denoted as a-Stokes, or simply aS). This field is generated simultaneously to the Stokes radiation being scattered by the interaction between the pump field and the optical phonons in silicon. In the case of the anti-Stokes wave, the phonon vibration in the material transfers energy to the electromagnetic field. The resulting wave then has a higher frequency than the pump wave, shifted by the same amount as the Stokes wave (15.6 THz for optical phonons in bulk silicon). Under no external influence on the vibronic state of the crystal, and standard equilibrium temperature conditions (up to 100 °C), the amount of a-Stokes radiation relative to the Stokes radiation is governed by a Boltzmann distribution, and is negligible for all practical purposes. However, the extent to which this assertion is true and the nature of the Raman process that occurs in the waveguide depend upon the phase mismatch between the pump (β_p), Stokes (β_S) and anti-Stokes (β_{aS}) waves, which is given as follows [40]:

$$\Delta\beta = 2\beta_p^{\mu_p} - \beta_s^{\mu_s} - \beta_{aS}^{\mu_{aS}} , \tag{22}$$

where β_λ^μ is the wave-vector for the given wavelength and the corresponding mode of polarization μ (1 for TE$_0$ and 2 for TM$_0$). As $\Delta\beta$ approaches zero, pump, Stokes and anti-Stokes waves experience a coherent interaction. This phenomenon is well known in the literature as Coherent anti-Stokes Raman Scattering (CARS) and can be explained in simple terms as the creation of anti-Stokes (Stokes) photons as a result of the coupling of two pump photons and one Stokes (anti-Stokes) photon, with the in-phase creation and annihilation of one zone-center optical phonon, as illustrated in Fig. 4. This interaction of the three fields, E_p, E_S and E_{aS}, is a Four-Wave-Mixing (FWM) process, and is governed by the third order nonlinear susceptibility in silicon, $\chi^{(3)}$. In general, the $\chi^{(3)}$ tensor has two contributions. The first is the "electronic", nonresonant component, $\chi_{NR}^{(3)}$, which is nearly instantaneous in response and hence broadband, and which accounts for such effects as self-phase modulation (SPM) and FWM. The second is the Raman component, $\chi_R^{(3)}(\Omega = \omega_p - \omega_S)$ which accounts for SRS and CARS. The $\chi_R^{(3)}(\Omega)$ component has a strong spectral dependence, with a resonant peak at $\Omega = \Omega_0$, the frequency of oscillation of zone-center optical phonons in silicon. The element $\chi_R^{(3)}(\Omega)$ has therefore the spectral signature of the Raman-active phonon modes of vibration of the crystal lattice. This implies that there is a response time associated with this component, which corresponds to the phonon de-phasing lifetime. In the case of first order Raman scattering from silicon at room temperature, where only zone-center optical phonons are involved, the bandwidth is ~ 105 GHz. This corresponds to a response time of about 10 ps. The details of CARS in silicon and how it applies to SOI waveguides will be worked out theoretically in the next two sections. Experimental demonstration of this phenomenon appears in Sect. 3.2.3.

2.5   Coupled-Mode Analysis of CARS in Silicon Waveguides

The evolution of the Stokes and the anti-Stokes waves coupled by the third-order susceptibility can be described according to Maxwell's equations by the following differential equations [30, 41]:

$$\frac{dE_S}{dz} = \eta_{11}E_S + \eta_{12}E_{aS}^* e^{i\Delta\beta z} , \tag{23a}$$

$$\frac{dE_{aS}^*}{dz} = -\eta_{22}E_{aS}^* - \eta_{21}E_S e^{-i\Delta\beta z} , \tag{23b}$$

where E_S and E_{aS} refer to the electric fields of the Stokes and anti-Stokes waves, respectively. The coupling coefficients can be written in terms of the nonlinear susceptibility and the pump electric field (E_p) as:

$$\eta_{11} = i\frac{k_S^2}{2\beta_S}\left(\chi_{NR}^{(3)} + \chi_R^{(3)}\right)|E_p|^2 , \qquad \eta_{12} = i\frac{k_{aS}^2}{2\beta_S}\left(2\chi_{NR}^{(3)} + \chi_R^{(3)}\right)E_p^2 , \tag{24a}$$

$$\eta_{22} = i\frac{k_{aS}^2}{2\beta_{aS}}\left(\chi_{NR}^{(3)} + \chi_R^{(3)}\right)|E_p|^2 , \qquad \eta_{21} = i\frac{k_S^2}{2\beta_{aS}}\left(2\chi_{NR}^{(3)} + \chi_R^{(3)}\right)E_p^2 , \tag{24b}$$

where $k_{s,aS} = \beta_{s,aS}/n_{s,aS}$. The steady state solution for the fields, in terms of their initial value at $z = 0$, can be written in the following form:

$$\begin{pmatrix} E_S(z) \\ E_{aS}(z) \end{pmatrix} = \begin{pmatrix} T_{11}\ T_{12} \\ T_{32}\ T_{33} \end{pmatrix} \begin{pmatrix} E_S(0) \\ E_{aS}(0) \end{pmatrix}, \tag{25}$$

where the transmission coefficients are:

$$T_{11} = e^{\eta_{11}z} \frac{s^- e^{s^+z} - s^+ e^{s^-z}}{s^- - s^+}, \tag{26a}$$

$$T_{12} = \eta_{12} e^{\eta_{12}z} \frac{e^{s^-z} - e^{s^+z}}{s^- - s^+}, \tag{26b}$$

$$T_{22} = e^{-\eta_{22}z} \frac{\lambda^- e^{\lambda^+z} - \lambda^+ e^{\lambda^-z}}{\lambda^- - \lambda^+}, \tag{26c}$$

$$T_{21} = -\eta_{21} e^{-\eta_{21}z} \frac{e^{\lambda^-z} - e^{\lambda^+z}}{\lambda^- - \lambda^+}, \tag{26d}$$

with

$$\lambda^\pm = s^\pm - i\Delta\beta + \eta_{22} + \eta_{33}, \tag{27a}$$

$$s^\pm = \frac{i\Delta\beta - \eta_{22} - \eta_{33} \pm \sqrt{(i\Delta\beta - \eta_{22} - \eta_{33})^2 - 4\eta_{23}\eta_{32}}}{2}. \tag{27b}$$

Exactly at the Raman resonance, $\chi_R^{(3)}$ is imaginary and $\chi_{NR}^{(3)}$ can be neglected. Then $\eta_{11} = g_R/2$, where g_R is the steady-state Raman gain, and to a good approximation $\eta_{11} \approx \eta_{22} \approx \sqrt{\eta_{12}\eta_{21}}$. The dispersion regime for which $2\eta_{22} \ll |\Delta\beta|$, is the region in which the Stokes wave is amplified and the Stokes-anti-Stokes coupling is highly suppressed. As $\Delta\beta \to 0, s^\pm \to -g_R$, and the Stokes and anti-Stokes fields can be approximated in the following form:

$$E_S(z) = E_S(0) + (E_S(0) + E_{aS}^*(0))g_R z/2,$$
$$E_{aS}^*(z) = E_{aS}^*(0) - (E_S(0) + E_{aS}^*(0))g_R z/2. \tag{28}$$

The solution predicts no change in the Stokes and anti-Stokes fields if the initial fields are equal in amplitude and opposite in phase. The above equation predicts a linear increase in the fields with distance, but this is valid under the assumption that $s^+ \approx s^-$, which holds true only for small propagation lengths. At lengths $z \sim 1/(s^+ - s^-)$, the difference becomes significant and leads to saturation of the fields. This characteristic length corresponds to tens of cm in silicon; therefore, this regime is not expected to occur in chip-scale devices. The physics of this saturation is the cancellation of the phonon oscillation amplitude, due to dephasing of the creation and annihilation events depicted in Fig. 4.

To illustrate the physical process described in (26d)–(28), Fig. 5 depicts the effective amplification coefficient of the Stokes (or a-Stokes) wave,
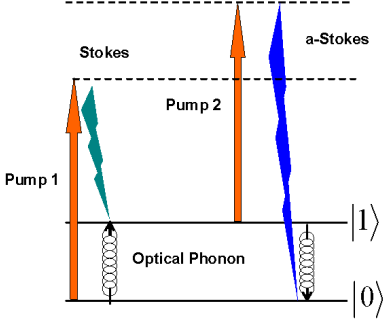
Fig. 4. Schematic energy-level diagram of the CARS process. Notice that the four photons involved are synchronized with the phonon oscillation that is created and reabsorbed in the process
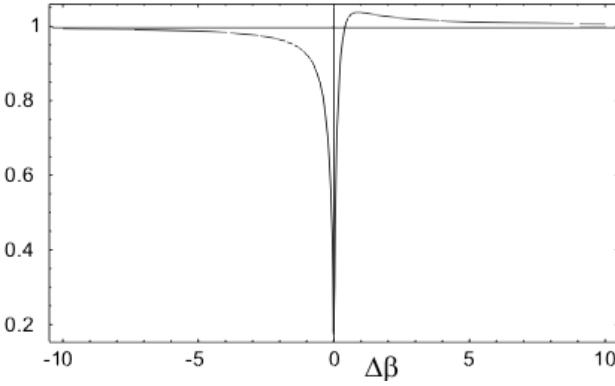
Fig. 5. The variation of normalized Raman gain as a function of the phase mismatch $(\Delta \beta \, \text{cm}^{-1})$

$A = \text{Im}(s^{\pm})$, normalized to the bulk SRS gain coefficient, g_{R}, as a function of the phase mismatch, $|\Delta \beta|$ [28]. At large values of $|\Delta \beta|$, SRS is the predominant effect and leads to the amplification of the Stokes signal with an effective gain that is very close to g_{R}. At small, negative values of $\Delta \beta$, the Stimulated Raman effect is considerably suppressed and the parametric coupling effects dominate. In this region, Stokes, anti-Stokes and pump fields are strongly coupled and parametric scattering, enabled through the Raman susceptibility, dominates. For small, positive values of $\Delta \beta$, the normalized gain slightly exceeds unity due to modulation instability. This effect has also been predicted and observed in optical fibers [40, 42].

2.6   Parametric Wavelength Converter

The power conversion efficiency between the Stokes and anti-Stokes waves, $|T_{12}|^2$ in (26d) as a function of the phase mismatch, $\Delta \beta$, is shown in Fig. 6,
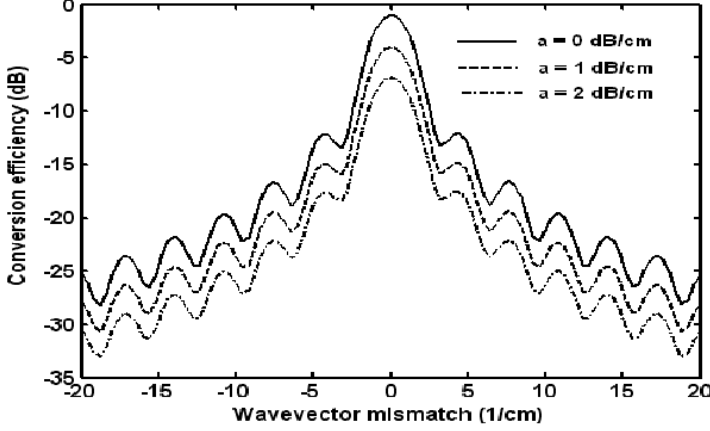
Fig. 6. Power conversion efficiencies (in dB) vs. wavevector mismatch for a 2 cm long waveguide of cross-section $4\,\mu\mathrm{m}^2$ and pump power of $400\,\mathrm{mW}$

with $400\,\mathrm{mW}$ of pump power effectively coupled into a waveguide of modal cross-section, $A = 4\,\mu\mathrm{m}^2$. The efficiency is plotted for different values of the propagation loss. In the following paragraph, we will consider the possibility of using the CARS effect to transfer information between the Stokes and anti-Stokes waves. The conversion efficiency of the wavelength converter is strongly dependent on the phase mismatch, as evident in Fig. 6.

From Fig. 6, the conversion efficiency is within 3 dB of the maximum value for a range of values of $\Delta\beta_{3\,\mathrm{dB}} = \pm 1.3\,\mathrm{cm}^{-1}$, around the phase matched condition.

An important parameter is the utility bandwidth, defined as the 3-dB bandwidth over which efficient conversion occurs. Clearly, an upper limit for the utility bandwidth is given by the Raman bandwidth itself, $2\Gamma = 105\,\mathrm{GHz}$. The utility bandwidth will depend on the bandwidth dictated by phase matching. To determine this, we need to introduce the detuning parameter, $\Delta\varpi$, defined in Fig. 7. The value of $\Delta\beta$ between the pump $(\beta_\mathrm{p}, \omega_\mathrm{p})$, Stokes $(\beta_\mathrm{S}, \omega_\mathrm{S} = \omega_\mathrm{p} - \Omega - \Delta\varpi)$ and anti-Stokes $(\beta_\mathrm{aS}, \omega_\mathrm{aS} = \omega_\mathrm{p} + \Omega + \Delta\varpi)$ signals, with differing polarizations and detuning, $\Delta\varpi$, around the Raman resonant frequency, will be calculated next. The dependence of $\Delta\beta$ on $\Delta\varpi$ will yield the utility bandwidth. Assuming that $\Delta\varpi \ll \Omega$ (which is quite reasonable for $\Delta\varpi < 105\,\mathrm{GHz}$, the total $\Delta\beta$ can be written as [30]:

$$\Delta\beta = 2\left(\beta_\mathrm{p}^\mu - \beta_\mathrm{p}^{*\mu}\right) - \left[\left(\frac{\mathrm{d}^2\beta_\mathrm{p}^{*\mu}}{\mathrm{d}\omega^2}\right)_\mathrm{mat} + \left(\frac{\mathrm{d}^2\beta_\mathrm{p}^{*\mu}}{\mathrm{d}\omega^2}\right)_\mathrm{wg}\right]\Omega(2\Delta\varpi - \Omega)$$

$$+ \Delta\beta_\mathrm{Raman}\,, \quad (29)$$

where β_p^μ and $\beta_\mathrm{p}^{*\mu}$ take into account the most general configuration between the polarization of the Stokes, pump, and a-Stokes fields. The effect of bire-
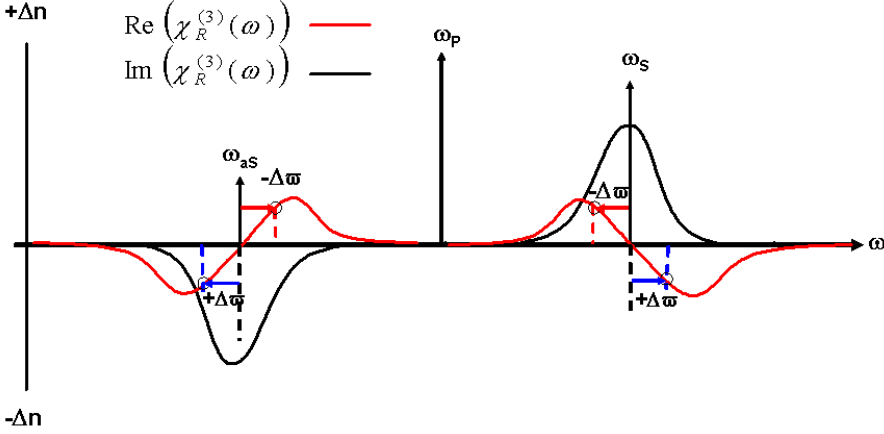
Fig. 7. Real and imaginary part of $\chi_R^{(3)}(\omega)$. The fact that $\mathrm{Im}(\chi_R^{(3)}(\omega_S)) = -\mathrm{Im}(\chi_R^{(3)}(\omega_{aS}))$, expressed in (28), gives rise to a nonzero Δn for a finite value of $\pm\Delta\varpi$. See text for details

fringence is taken into account in the first term of (23a). The second term groups together the effect of material and waveguide dispersion around the Raman-resonant frequency. The last term denotes the excess phase-mismatch arising from the real part of the Raman susceptibility. The real part of the Raman susceptibility leads to changes in the refractive index, Δn, when the Stokes and a-Stokes frequencies are slightly detuned off the Raman resonance. Both changes (Stokes and a-Stokes index) have the same sign [43], and therefore, their contributions to $\Delta\beta$ add up, to effectively introduce a total nonzero phase-mismatch around the resonant wavelength; this is clearly depicted in Fig. 7. The term $\Delta\beta_{\mathrm{Raman}}$ can be expressed as:

$$\Delta\beta_{\mathrm{Raman}} = \frac{2\omega_p\Delta n}{c}, \tag{30}$$

$$\Delta n = \frac{\chi_{\mathrm{real}}^R(\Omega - \Delta\varpi)|E_p|^2}{2n} = -\frac{\xi_R I_p}{2cn^2\varepsilon_0}\left(\frac{\Delta\varpi/\Gamma}{1+(\Delta\varpi/\Gamma)^2}\right), \tag{31}$$

where $|E_p|^2 = \frac{I_p}{2cn\varepsilon_0}$ [43], and $\xi_R = -11.2 \times 10^{-14}\,\mathrm{cm}^2/\mathrm{V}^2$ (cf Sect. 2.2). The bandwidth of the process can be defined in terms of $\Delta\beta_{3\,\mathrm{dB}}$ by the condition $|\Delta\beta| < \Delta\beta_{3\,\mathrm{dB}}$. The contribution of detuning, $\Delta\varpi$, to $\Delta\beta$, via material and waveguide dispersion, contained in the second term of (29), has the following values:

$$(\mathrm{d}^2\beta_{\mathrm{TM}}/\mathrm{d}f^2)_{\mathrm{wg}} = -3.5 \times 10^{-2}\,\mathrm{THz}^{-2}\cdot\mathrm{cm}^{-1}, \tag{32}$$

$$(\mathrm{d}^2\beta_{\mathrm{TM}}/\mathrm{d}f^2)_{\mathrm{mat}} = 0.48 \qquad \mathrm{THz}^{-2}\cdot\mathrm{cm}^{-1}. \tag{33}$$

These values were obtained from simulations performed with commercial mode-solving software for the specific SOI waveguide described in the previous paragraphs (Fimmwave$^{\mathrm{TM}}$ Version 4.1.6). It is clear from (32) and (33)
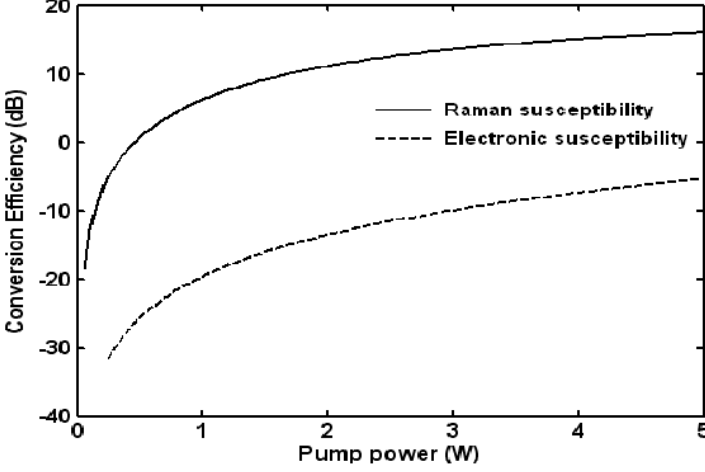
Fig. 8. Power conversion efficiency (in dB) for the Stokes to Anti-Stokes conversion via the Raman susceptibility and Electronic susceptibility for a waveguide 2 cm long and with $4\,\mu\text{m}^2$ cross-sectional area

that, for $\Delta\varpi < \Gamma$, the contribution of the material and waveguide dispersion to $\Delta\beta$ is much smaller than $\Delta\beta_{3\,\text{dB}}$. Then, the only contribution to $\Delta\beta$ that needs to be considered is that coming from $\Delta\beta_{\text{Raman}}$, (30) and (31). The result is a utility bandwidth that is limited by the input pump intensity (and therefore, conversion efficiency). For values of pump intensity, $I_{\text{p}} < 35\,\text{MW/cm}^2$ (1.4 W effectively coupled into a waveguide of the dimensions considered here), $\Delta\beta_{\text{Raman}}$ is negligible and the utility bandwidth is still $2 \times \Gamma$ ($= 105\,\text{GHz}$). At higher pump intensities, $\Delta\beta_{\text{Raman}}$ becomes the limiting factor, e.g. at $100\,\text{MW/cm}^2$ the total utility bandwidth has been reduced to 18 GHz.

At this point, it is instructive to compare the relative contributions to the conversion process due to each of the terms, $\chi_{NR}^{(3)}$ and $\chi_{R}^{(3)}$, in silicon. Figure 8 shows the Stokes-to-a-Stokes conversion efficiency for each component, and it is clear that, in silicon waveguides, the Raman susceptibility dominates the process by approximately 20 dB, regardless of the pump power value.

Wavelength conversion can also be performed using the nonresonant third-order susceptibility in an optical fiber, as shown in Fig. 9a. However, the nonresonant susceptibility, since it is a broadband contribution, also causes cross talk between adjacent WDM channels. In contrast, the conversion in silicon, shown in Fig. 9b, is performed by the Raman susceptibility which, in addition to being much more efficient than its nonresonant counter part, does not result in cross talk. This represents a fundamental difference between conversion in silicon and that in fiber.
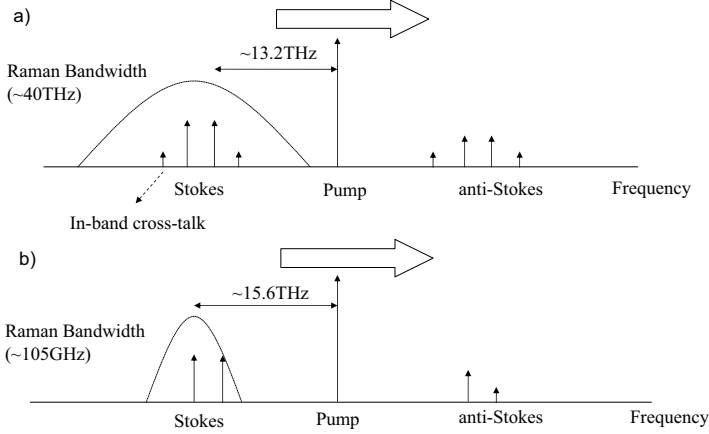
Fig. 9. Pictorial description of the parametric conversion process and the effect of cross-talk. (**a**) In silica fibers, FWM is dominant over CARS. FWM leads to cross-talk between adjacent channels. (**b**) In silicon waveguides, CARS is the dominant effect. The CARS process leads to parametric conversion to the anti-Stokes spectrum, with negligible cross-talk due to CARS and/or FWM. The laser sources are assumed to be monochromatic and the frequency axis is not drawn to scale

2.7 Phase Matching by Dispersion Engineering in Silicon Waveguides

The variation of the power conversion efficiency with phase mismatch, as depicted in Fig. 6, clearly shows that the conversion efficiency of the wavelength converter is strongly dependent on the phase mismatch. The various contributions to the phase mismatch have been considered in (29). In this section, we will focus on the design of the rib waveguide dimensions and choose the pump, Stokes and anti-Stokes wavelengths in such a way that perfect phase matching is achieved and the conversion efficiency is maximized. Material dispersion can be modelled based on the refractive index variation with wavelength for silicon, as given by the following expression [44]:

$$n^2 = \varepsilon_1 + \frac{A}{\lambda^2} + \frac{B\lambda_1^2}{\lambda^2 - \lambda_1^2} , \tag{34}$$

where $A = 0.939816$, $B = 8.10461 \times 10^{-3}$ and $\lambda_1 = 1.1071\,\mu\text{m}$. The third term is the contribution of the indirect band-gap and the first two represent contributions from all other resonances. The phase mismatch contribution due to material dispersion is graphically represented in Fig. 10. To a good approximation, the phase mismatch is dependent only on $\text{d}^2\beta/\text{d}\omega^2$. Since we are concerned with wavelengths below the band-gap, the dispersion is normal and phase mismatch is negative.

The effect of waveguide dispersion was characterized by numerical simulations, and the phase mismatch is calculated to be within $+5$ and $-15\,\text{cm}^{-1}$
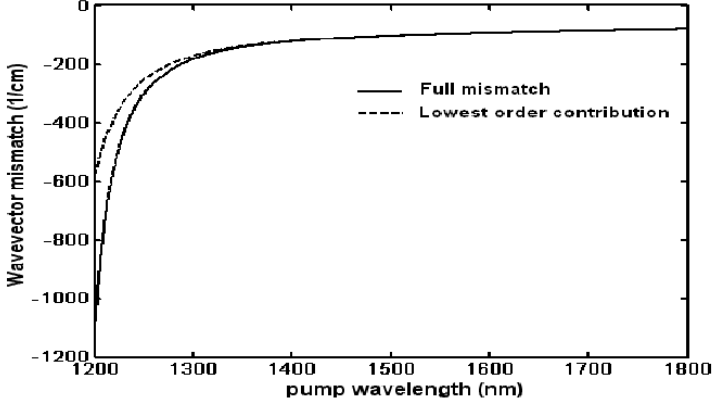
Fig. 10. Phase mismatch contribution (cm^{-1}) due to material dispersion, as a function of wavelength

for the range of waveguide dimensions described below (see Fig. 12). These values are insufficient to cancel the effect of material dispersion. As mentioned earlier, the phase mismatch due to SPM and XPM is also very small and insignificant compared to material dispersion. When the pump is launched in orthogonal polarization relative to the signal (both Stokes and anti-Stokes), the contribution of the birefringence term can be in the range $-600\,\mathrm{cm}^{-1}$ to $600\,\mathrm{cm}^{-1}$, depending on the waveguide dimensions and the polarization configuration. However, the birefringence of the waveguide, $D = \beta^{\mathrm{TM}} - \beta^{\mathrm{TE}}$, can be conveniently engineered by adjusting the waveguide dimensions. Figure 11 shows a schematic representation of the dispersion curves for the TE_0 and TM_0 modes of a typical silicon waveguide. The three wavelengths, λ_{p}, λ_{aS} and λ_{s}, are indicated. In general, D is wavelength dependent, but it can be assumed constant for the sake of simplicity. The value of $\Delta\beta$ for the configuration in which the pump field is coupled in the TE_0 mode, with the Stokes and a-Stokes fields coupled into the TM_0 mode, is labelled $\Delta\beta_1$, and its different components are given by the orange marks in the figure. The opposite configuration, with the pump field coupled into the TM_0 mode and the Stokes, a-Stokes fields coupled into the TE_0 mode, has a total phase mismatch $\Delta\beta_2$, and its components are marked in blue.

It can be easily seen that, in general, $\Delta\beta_2 < \Delta\beta_1$, and the amount by which these two values are different is $\sim 4D$. Since the value of D depends on the waveguide design, it is possible to design a waveguide such that $\Delta\beta_1 = 2D$, and $\Delta\beta_2 = -2D$. Under these conditions, the device will be a polarization-independent wavelength converter, as can be deduced by the symmetry of both SRS and CARS effects, relative to $\pm\Delta\beta$ (see Figs. 5 and 6). The conversion efficiency of the device can be adjusted by choosing a small value of D. Achieving this phase matched condition requires careful design of the waveguide dimensions. Figure 12 shows the plot of total
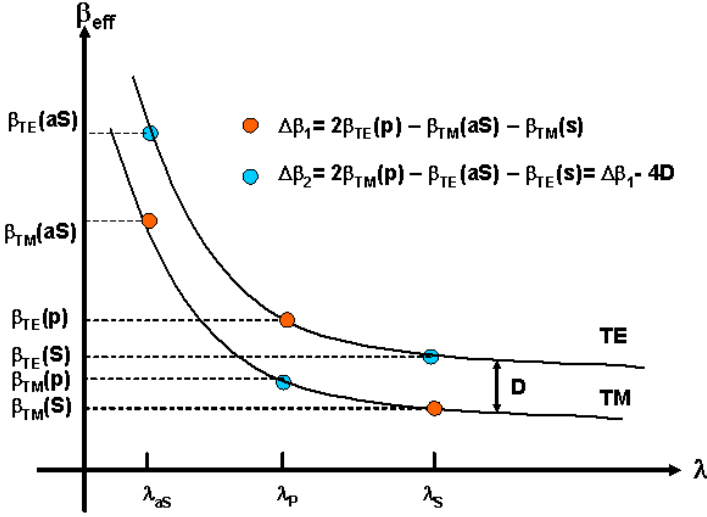
Fig. 11. Schematic representation of birefringence in the CARS effect. The indexes are: P-pump field, S-Stokes field, and aS-anti-Stokes field. See text for details
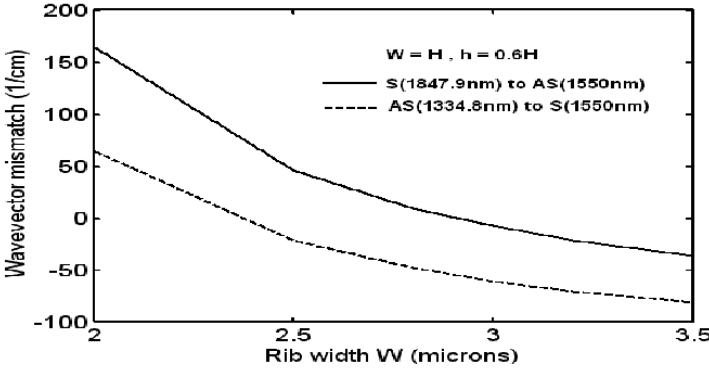

Fig. 12. Total momentum mismatch vs. dimension increase for both Stokes (1847.9 nm) to Anti-Stokes (1550 nm) (*solid line*) and Anti-Stokes (1334.8 nm) to Stokes conversion (1550 nm) (*dashed line*)

phase mismatch as a function of one of the rib dimensions, obtained by simulation [29, 30]. These results were obtained for waveguides with $w = H$ and $h = 0.6H$, with the rib width varied from 2 μm to 3.5 μm and for two different cases of wavelength combinations. These dimensions satisfy the single mode propagation condition. The solid line shows the phase mismatch for Stokes to anti-Stokes conversion from 1847.9 nm to 1550 nm respectively, and the dashed line shows the phase mismatch for anti-Stokes to Stokes conversion from 1550 nm to 1334.8 nm. Phase matching is achieved at an optimum rib width of 2.9 μm and 2.35 μm in the above cases, respectively.
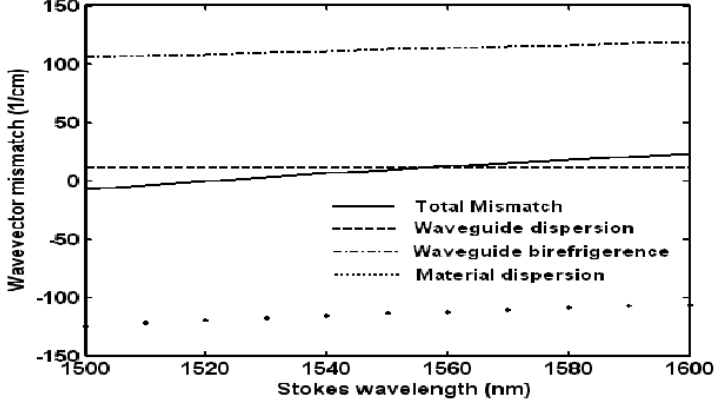
Fig. 13. Momentum mismatch for waveguide $w = H = 2.3\,\mu\text{m}, h = 0.6H$ versus wavelength in CARS: total mismatch (*solid line*), material dispersion contribution (*dotted line*), waveguide dispersion contribution (*dashed line*) and birefringence contribution

The variation of the total phase-mismatch as a function of the Stokes wavelength is shown in Fig. 13, for a waveguide with $w = H = 2.3\,\mu\text{m}$ and $h = 0.6H$. The calculations were performed by adjusting the pump and a-Stokes wavelength such that, for every value of the Stokes frequency, the following is true: $\omega_\text{p} - \omega_\text{s} = \omega_\text{aS} - \omega_\text{p} = \Omega \; (= 15.6\,\text{THz})$. The Stokes wavelength is varied between 1500 nm–1600 nm, and phase matching is achieved around 1520 nm, with the corresponding anti-Stokes wavelength around 1312 nm. The contribution of each of the components to the total phase mismatch is shown in the figure. The calculated waveguide dispersion is found to be almost constant over the entire wavelength range. It is important to analyze the effect of deviations of the waveguide dimensions due to fabrication errors on the phase matching condition. Deviations in waveguide width can arise due to error in the mask features and the improper transfer of the pattern during lithography. Uncertainties in etching and undercutting could lead to error in the rib/slab heights. The effect of these uncertainties on the phase mismatch is graphically depicted in Fig. 14. For the mismatch to remain within $\pm 1.3\,\text{cm}^{-1}(= \Delta\beta_{3\,\text{dB}})$, it is required that the variations in waveguide width and slab height be within 70 nm and 10 nm, respectively. As a benchmark, the transistor gate length in CMOS circuits going into production next year is 70 nm, with ± 7 nm of accuracy. Therefore, the dimensional accuracy required for achieving phase matching in silicon waveguides is within the tolerance of the silicon manufacturing process.

In conclusion, waveguide engineering provides a powerful tool to maximize the efficiency of nonlinear optical phenomena in silicon microstructures. In the following section, the experimental realization of the ideas discussed up to now, will be described.
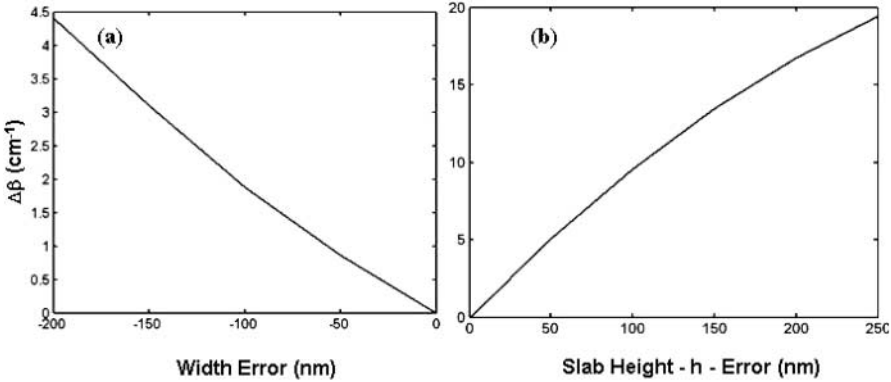
Fig. 14. Variation of phase mismatch with deviation in waveguide dimensions (**a**) Rib width (nm) (**b**) Slab height (nm)

3   Experimental Results

### 3.1   Spontaneous Raman Scattering Observed in Silicon Waveguides

The experimental setup used to observe Spontaneous Raman Scattering in silicon waveguides is shown in Fig. 15. The pump laser is a high power fiber laser that delivers CW, randomly-polarized light, at 1427 nm, with a 2 nm linewidth at maximum power.

The selected scattering configuration combines a large relative Raman efficiency (see Table 1), with orthogonal pump and signal polarizations. The orthogonal configuration satisfies the Raman selection rules for scattering from a silicon crystal oriented with its $[1\bar{1}0]$ axis along the beam propagation direction, and is helpful for signal-pump isolation at the output. In order to
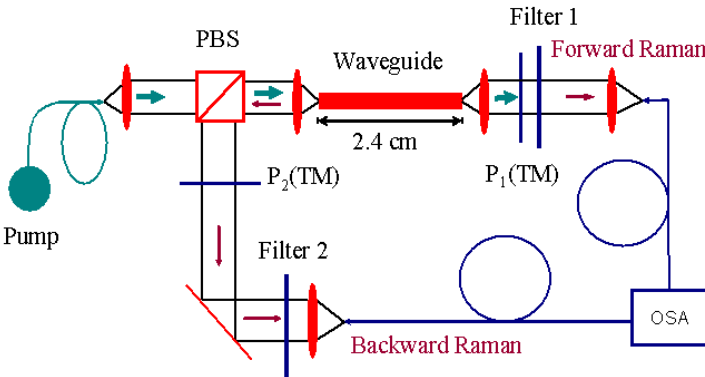
Fig. 15. Experimental setup for measurement of spontaneous Raman scattering from silicon waveguides
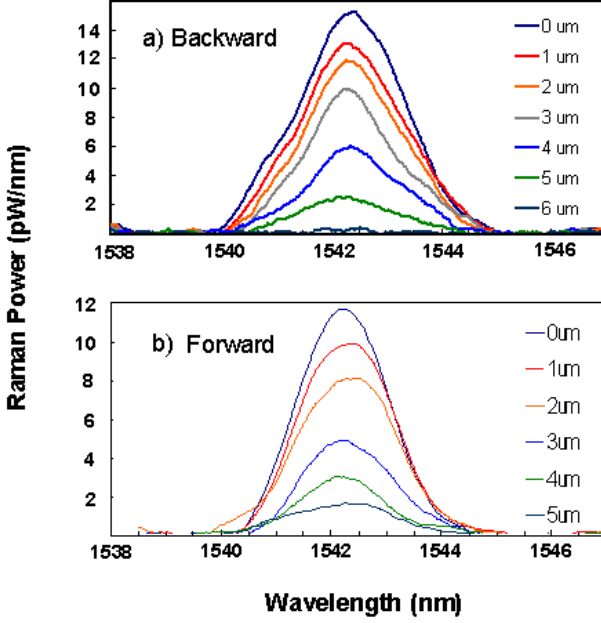
Fig. 16. Raman spectra from silicon obtained for different horizontal offsets of the waveguide relative to the optical axis. (**a**) shows the back-scattered spectra, and (**b**) shows the forward-scattered spectra

realize this configuration, a Polarization Beam Splitter (PBS) was used to split the pump beam into S and P polarized beams. The P-polarized beam is sent into the waveguide and acts as the TE_0-mode Raman pump. The Raman signal backscattered from the waveguide (TM_0 mode) is collected from Port 2 of the PBS. For further signal filtering and background rejection, a polarizer (P_1), and a 1530 nm–1550 nm bandpass filter (Filter 1) are placed before the collection fiber port in Port 2. A polarizer (P_2) and a bandpass filter (Filter 2) remove the pump signal and pass the backward scattered radiation into another collection fiber port. The silicon rib waveguide used is shown in Fig. 2. The waveguide for this particular experiment has a 5 μm width (w) and 2.5 μm rib height (h), with a 5 μm total thickness (H).

Figure 16 shows the experimental results obtained in both forward and backward scattering configurations. All the spectra are shifted by 15.6 THz from the pump laser line (at 1427 nm), and therefore, belong to the spontaneous Raman signal from zone-center optical phonons in bulk silicon. The different spectra on each of the Fig. 16a and b correspond to displacements of the waveguide in the plane perpendicular to the optical axis of the experimental setup shown in Fig. 15. The rapid decrease in the signal as the waveguide is displaced by 2 μm or 3 μm, either laterally or vertically, proofs that the signal collected comes directly from the bulk of the SOI waveguide,
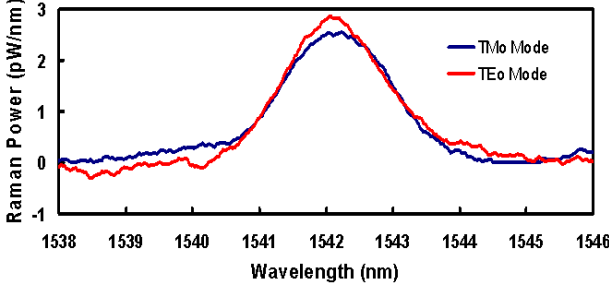
Fig. 17. Raman spectra from SOI waveguides obtained by rotating the polarizer P1 (Fig. 15) by 90°. The scattering intensity is essentially the same, as expected from the selection rules

and not from the front-end facet of the silicon chip. The selection rules, discussed in Sect. 2.1, can also be easily verified using the experimental setup shown in Fig. 15. The Raman scattering intensity, collected from the TM_0 and the TE_0 modes of the waveguide, can be obtained by simply rotating the polarizer P_1 over 90°. The result is shown in Fig. 17, where it can be seen that the scattering intensity is the same in both polarizations.

The fact that the absolute intensity of Forward and Backward Raman scattering are comparable, as shown in Fig. 16, is expected from bulk Raman scattering. Other authors have found a surprising asymmetry between the two processes in GaP waveguides, and attributed it to phonon confinement effects introduced by the waveguide structure [45]. These effects should have no role in the case of silicon waveguides, because in silicon the three optical modes participate equally in the first-order Raman process. However, if the Raman intensities are plotted as a function of the pump power intensity, a clear asymmetry is found between Forward and Backward scattering, as shown in Fig. 18. The origin of this asymmetry has to be related to the waveguide propagation losses, rather than coupling losses, since the latter affect both directions of propagation in a symmetric fashion. In the case of spontaneous Raman scattering, the equations that govern the propagation of pump ($P_P(z)$) and signal ($P_R(z)$) field power along the waveguide are obtained in a manner similar to [46], but with the effect of the stimulated emission term omitted. This is validated since the low value of the Raman signal measured clearly shows that the experiment was performed well within the linear regime in silicon. The CMC theoretical approach discussed in Sect. 2.3, demonstrates that there is no inter-modal coupling within the waveguide; therefore, in the following derivation only the intensity of the fields will be considered, in the usual manner. The expressions for $P_P(z)$ and $P_R(z)$ are then,

$$P_P(z) = P_P(0)e^{-\gamma z}, \tag{35}$$

$$\frac{dP_R(z)}{dz} = \mp\gamma P_R(z) \pm \alpha P_P(z), \tag{36}$$

where the upper (lower) sign in (36) applies in forward (backward) scattering. Here, γ is the propagation loss of the waveguide in units of cm^{-1}, and α is the spontaneous Raman coefficient for the silicon waveguide, defined as:

$$\alpha = S \Delta \Omega . \tag{37}$$

with S the Raman scattering efficiency $(\text{cm}^{-1} \cdot \text{sr}^{-1})$ in silicon at $1542\,\text{nm}$, as defined in Sect. 2.1. The factor $\Delta \Omega$ is the effective solid angle of collection for the TM_0 waveguide mode, and is measured to be $\Delta \Omega = 0.013\,\text{sr}$. The model used to obtain (35) and (36) is actually a simplification of the real optical field propagation along the waveguide, and assumes that the field has already been coupled into a single-mode. In reality, the situation is quite different, since the parameter γ turns out to be a function of the propagation length, $\gamma(z)$. Modeling of this effect is out of the scope of the present work, but measurements can be accurately done using well known, infrared scattering measurement techniques [47]. For the purpose of the present discussion, we will keep the model from (35), in the understanding that the parameter γ is rather an "effective" or averaged value of the propagation loss along the waveguide. The total Raman signal power, P_{R}, measured either in forward configuration (at the output end of the waveguide) or in backward configuration (from Port 2 in the PBS) is related to the pump power at the input facet of the waveguide (P_{P}) by integrating (35) and (36), with the following result:

Backward: $P_{\text{R}} = \alpha \left(\dfrac{1 - e^{-2\gamma L}}{2\gamma} \right) P_{\text{P}} ,$ \hfill (38)

Forward: $\quad P_{\text{R}} = \alpha L e^{-\gamma L} P_{\text{P}} ,$ \hfill (39)

where L is the length of the waveguide. From (38) and (39), it is seen that the ratio between the slopes of the lines in Fig. 18, m, can be related to γ (in the low propagation loss limit) by

$$m = \frac{\sinh(\gamma L)}{\gamma L} , \tag{40}$$

with the value of m obtained from Fig. 17 and using (40), we get an estimate for the propagation loss, $\gamma = 0.64\,\text{cm}^{-1} = 2.8\,\text{dB/cm}$. Note that the value thus obtained is independent of the Raman scattering coefficient and the optical coupling efficiency. It is expected that the value for propagation losses obtained using the Raman method would give an over-estimate. The reason for this is that the mode-coupling loss mentioned above also contributes to a larger backward scattering efficiency. This is because the scattered Raman light is more likely to be collected in the backward direction, since it is not effectively coupled to the waveguide in the forward direction. Other traditional methods to measure propagation loss of the single-mode along the waveguide, like cut-back techniques, result in lower values. Including this value of γ into (39) and using the measured slope in Fig. 18, with further
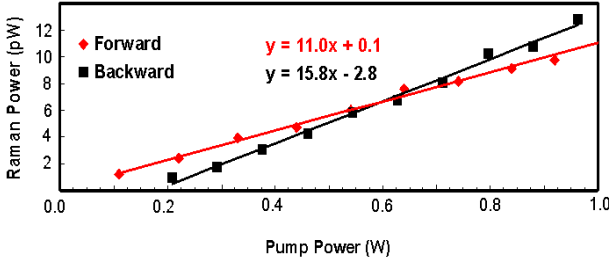
Fig. 18. Spontaneous Raman intensity as a function of pump power. Forward and backward scattering cases are shown. The pump power was measured between the PBS and the input coupling lens

correction for the back-scattering collection losses and waveguide coupling losses (20 dB total), a value is obtained of $\alpha = (5.3 \pm 3.2) \times 10^{-9}\,\mathrm{cm}^{-1}$. This is remarkably close to the values obtained above using the CMC formulation (cf the last two columns in Table 2). Notice that the values listed there correspond to waveguides with a total rib height of $H = 4.3\,\mu\mathrm{m}$, as compared to the $5\,\mu\mathrm{m}$ rib waveguide used in this experiment. With the above value for $\Delta\Omega(0.013\,\mathrm{sr})$, the scattering efficiency in silicon is obtained to be $S = (4.1 \pm 2.5) \times 10^{-7}\,\mathrm{cm}^{-1}\cdot\mathrm{sr}^{-1}$. The difference (a factor of 2), with the value obtained by *Ralston* and *Chang* for bulk silicon [35], should be related to the modal coupling losses in the waveguide, as discussed above. Indeed, as the high power pump laser impinges on the front facet, it propagates with high losses through the first few millimeter inside the silicon waveguide, before coupling into the single TE_0 mode. This means that, for most of the length of the waveguide, the effective pump laser power is less than assumed in the calculations, therefore reducing the value of the measured scattering coefficient.

3.2 Third-order Optical Nonlinearities in Silicon Waveguides

In bulk silicon, due to the crystal symmetry, second-order nonlinearities are highly suppressed, but third order nonlinearities may be observable if the field intensities used to generate them are high enough. In what follows, the three third-order optical nonlinearities in silicon, which have been treated theoretically above, will be demonstrated experimentally in silicon waveguides. These processes are: Stimulated Raman Scattering (SRS), Two-Photon Absorption (TPA), and Coherent Anti-Stokes Raman Scattering (CARS). The results confirm the values obtained from third-order nonlinear properties of bulk silicon.
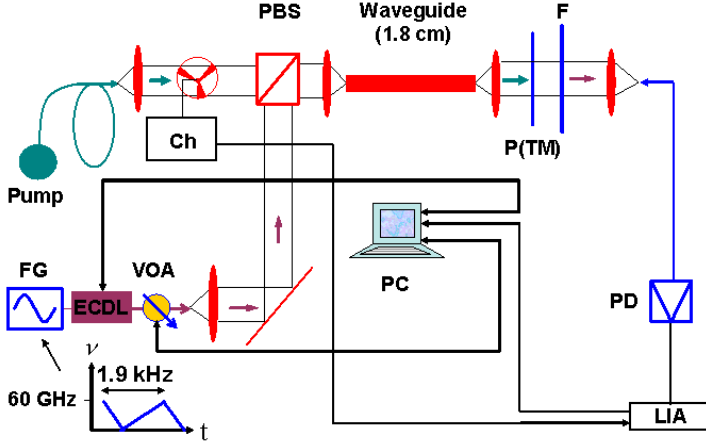
Fig. 19. Experimental setup: Pump-CRC fiber laser; Ch-Chopper; PBS-Polarization Beam Splitter; LIA-Lock-in amplifier; ECDL-External cavity diode laser (tunable); FG-Function generator (60 GHz freq. range); VOA-Variable optical attenuator; PD-optically-broadband photodetector. The *thick lines* represent electrical connections and wiring, the *thin lines* represent free-space optical beams, and the *colored lines* represent optical fiber. The SOI rib waveguides used for this experiment have a length, $L = 1.8\,\text{cm}$, and a measured TM_0 modal area of $a = 5.4\,\mu\text{m}^2$

3.2.1   Observation of Stimulated Raman Scattering in Silicon Waveguides

Figure 19 shows the experimental setup used to measure SRS in SOI waveguides. The pump laser is the same as described in the previous section. In the present case, the S-polarized input of the PBS is used to couple the signal beam into the TM_0 mode of the waveguide. The signal laser is an External Cavity Diode Laser (ECDL) with a linewidth of $< 300\,\text{kHz}$. The laser wavelength was scanned ($0.2\,\text{nm/step}$) through a wavelength range from $1537.0\,\text{nm}$ to $1547.0\,\text{nm}$. A variable optical attenuator (VOA) was used to regulate the amplitude of the signal beam. A polarizer (P) and a high pass filter are used to collect the field from the TM_0 mode coupled out of the waveguide.

To isolate the pump and signal interaction, a low frequency amplitude modulation is introduced in the pump beam, using a chopper (Ch) operating at $100\,\text{Hz}$. In the presence of a nonlinear interaction between pump and signal beams in the waveguide, this modulation will be transferred onto the CW signal beam. The interaction should possess the spectral characteristics of the Raman Effect. Given the $1427\,\text{nm}$ pump used in our experiment, and the $15.6\,\text{THz}$ optical phonon frequency, the gain bandwidth is expected to be centered at $1542.3\,\text{nm}$. An optically-broadband photodetector (PD) is used to measure the signal modulation. The signal from the PD is processed by a lock-in amplifier (LIA), which is locked to the chopper frequency.
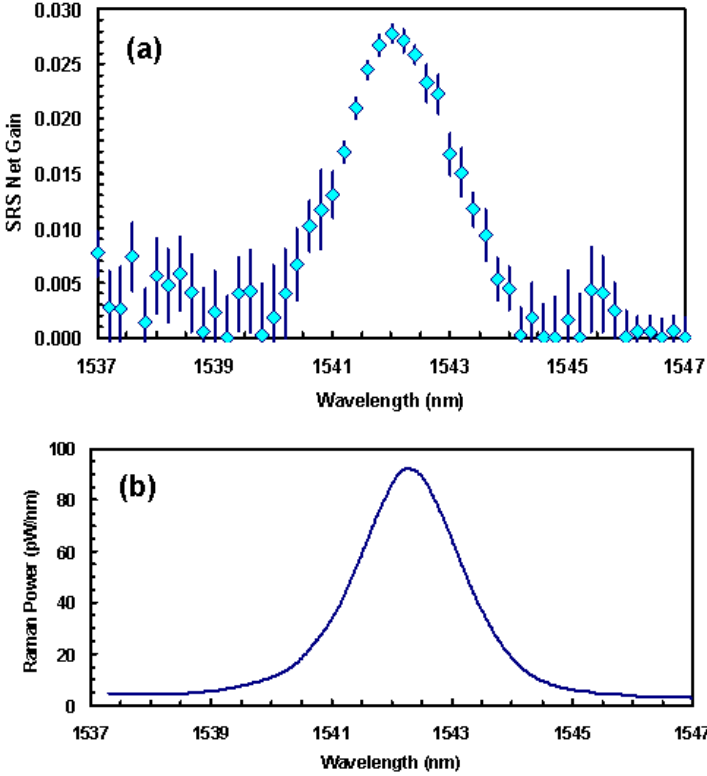
Fig. 20. (**a**) Measured spectral characteristic of the Stimulated Raman Scattering (SRS) in the silicon waveguide. The *error bars* are the standard deviation from 10 averages per point. The pump power was 0.64 W at the front facet of the waveguide. SRS Net gain is the ratio of the amplitude of the LIA output to the average signal power throughput. (**b**) Spontaneous Raman Spectra of the same waveguide with the same pump power as in (**a**), collected with an OSA

A function generator (FG) was used to modulate the ECDL frequency. The purpose of this is to average out the Fabry–Perot (FP) fringes produced by the waveguide facets, which are not AR coated. Shown in Fig. 20a is the measured signal power gain as a function of signal laser wavelength. The pump power, measured before the waveguide, was 0.64 W. The characteristic wavelength dependence of the Raman process is clearly shown, and a signal amplification of 3% is obtained. For comparison, shown in Fig. 20b is the measured spontaneous emission. The gain peak in the stimulated emission occurs at 1542.3 nm, as expected. Additionally, the FWHM linewidth of 310 GHz is consistent with the measured value for spontaneous emission.

In Fig. 21, the maxima of the signal wavelength scans are plotted versus the effective pump power. The maximum signal gain obtained is 0.25 dB, corresponding to ∼ 6% signal amplification. The slope of the curve is approx-
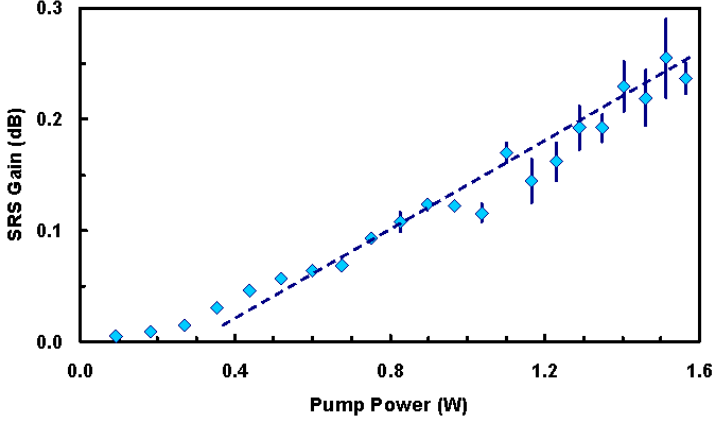
Fig. 21. The maxima from each spectral scan are plotted against effective pump power coupled into the front facet of the waveguide. A maximum of 0.25 dB (6%) amplification is obtained

imately linear, as expected for the gain of a Raman amplifier as a function of pump power.

The amplified signal power expected from a waveguide of length, L, given by (10), should be adjusted to accommodate for the pump broadening of the Raman signal, as follows,

$$P_S(L) = P_S(0) \, \exp\left(-\gamma \, L \, + \, \frac{g_R \, P_p(0)}{A \times (1 + \Delta\nu_p(P_p)/\Delta\nu_R)} L_{eff}\right). \qquad (41)$$

The factor $(1 + \Delta\nu_p/\Delta\nu_R)$ is an approximation describing the increase in Raman threshold due to the finite linewidth of the pump laser. The dependence of threshold on pump linewidth is well known in Stimulated Brillouin Scattering (SBS) in optical fibers [40]. Because of the extremely large Raman bandwidth in fibers (5 THz–10 THz), this effect is neglected in modelling SRS in fibers. However, due to the narrow Raman linewidth in silicon ($\Delta\nu_R = 105$ GHz), the dependence of threshold on pump linewidth must be considered here. Additionally, the linewidth, $\Delta\nu_p$, of the pump laser increases with output power. Based on the specifications provided by the manufacturer [48], the dependence of linewidth with pump power can be assumed to be linear, with a rate of 70 GHz/W. By using the total Stokes amplification obtained experimentally, in (41), a value of $g_R = 2 \times 10^{-8}$ cm/W is found for the SRS gain coefficient. As described in Sect. 2.1, the value obtained by using the measured waveguide spontaneous scattering efficiency and (9), is $g_R = 3.7 \times 10^{-8}$ cm/W, in good agreement with the present measurement. Other nonlinear optical effects may be detrimental to SRS. A serious problem for fiber-based Raman amplification is presented by SBS. However, the Brillouin scattering coefficient for silicon is about two orders of magnitude smaller than the Raman coefficient [49]. Furthermore, as has been discussed above,

the pump broadening reduction of the effective SBS gain is more pronounced than in the SRS case, due to the smaller bandwidth of the Brillouin signal. In conclusion, the possibility of SBS pump depletion in SOI-based Raman amplification schemes should be discarded. The hypothesis of two-photon-absorption quenching the SRS amplification measured above, as outlined in Sect. 2.2, should be ruled out by direct measurement of TPA in SOI wave-guides. This will be the topic of the following section.

3.2.2   Two-Photon Absorption in Silicon Waveguides

Two-Photon Absorption has been recognized as a detrimental factor in the operation of SOI optical devices in the telecommunications C-band (1.52 µm–1.58 µm), particularly causing pump-power depletion in waveguide-Raman amplifiers (see Sect. 2.2), and also through induced cross-talk in DWDM devices [50]. However, TPA in silicon has been effectively used at these wavelengths for diverse purposes, like implementing optical-beam-induced-current imaging techniques, used in IC failure analysis [51], and ultrafast sampling systems [52,53]. The TPA coefficient has been measured in silicon at 1.06 µm [54,55], but there have been very few reports in the 1.5 µm wave-length region [50,56]. Furthermore, theoretical efforts to calculate TPA at different wavelengths have been concentrated on III–V and II–VI semiconductors [57], which present a direct band-gap transition. The indirect transition involved in TPA for silicon, at the 1.5 µm region, requires the treatment of a phonon-assisted electronic process, which complicates the analysis. In this context, the availability of experimental data for TPA in silicon at 1.56 µm becomes of practical importance. It supports recently measured data in this wavelength region, providing relevant information with which theory can be compared, and settling the ground for the practical use of nonlinear effects in silicon.

The experimental setup used for this measurement is depicted in Fig. 22. A passively mode-locked laser operating at a 25 MHz pulse-repetition rate, and with a 0.9 ps pulsewidth, produces an input power level an order of magnitude higher than those used in previous reports of TPA in silicon [50, 56]. The laser operates at a center wavelength of $\lambda = 1560$ nm, which is well below the indirect band-gap of silicon; therefore, linear absorption can be considered negligible. The regime that this experiment then explores is that of indirect, simultaneous two-photon absorption [55]. Such an effect is of interest for ultrafast photodetection in silicon.

Shown in Fig. 23 is a plot of the throughput peak power, P_{out} as a function of the input peak power, P_{in}. The effect of the nonlinear absorption is clearly visible for input power levels above 50 W. This is more than an order of magnitude higher than the power levels used to observe SRS.

Under TPA-dominating conditions, the input power at the front facet of the waveguide, P_{in}, and the signal measured on PD_2, namely, P_{out}, are related
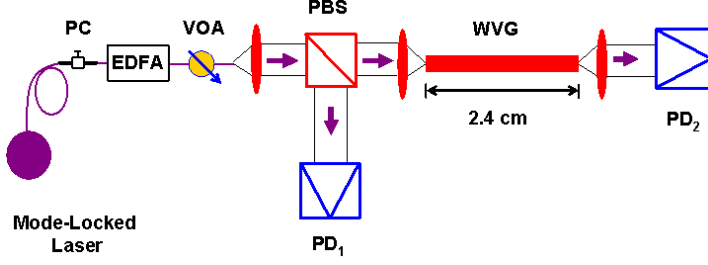
Fig. 22. Experimental setup for measuring TPA. The waveguide in this case is different from the one used for SRS. PC-Polarization controller; VOA-Variable optical attenuator; PBS-Polarization beam splitter; PD1 and PD2 photodetectors
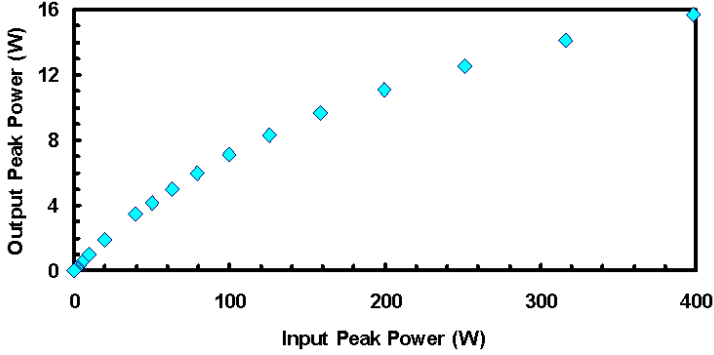
Fig. 23. Output power vs. input power results, using a mode-locked laser, and depicting a nonlinear relationship

by the following expression [55],

$$\frac{P_{\text{in}}}{P_{\text{out}}} = e^{\gamma L}\left(1 + \frac{BL_{\text{eff}}}{A}P_{\text{in}}\right),\tag{42}$$

where $\gamma = 0.46 \pm 0.1\,\text{cm}^{-1}$) is the propagation loss in the waveguide, A is the modal cross section ($= 8.1 \pm 1.0 \times 10^{-8}\,\text{cm}^2$), and B is the TPA coefficient (in cm/W). The result is plotted in Fig. 24, where the linear behavior of $P_{\text{in}}/P_{\text{out}}$ versus P_{in} is clearly demonstrated up to 400 Watt of input peak power. The fact that spontaneous TPA in silicon is the dominant absorption process up to such high power regimes, in the 1.5 μm region, is of fundamental importance in the design of an ultrafast silicon photodetector and/or imaging device. The resulting value for B is then,

$$B = -\frac{c_1 A}{L_{\text{eff}}}e^{-\gamma L} = (4.4 \pm 1.0) \times 10^{-10}\,\text{cm/W},\tag{43}$$

where c_1 is the slope of the curve shown in Fig. 24 and the main elements in the error are the uncertainties in γ, and in A.
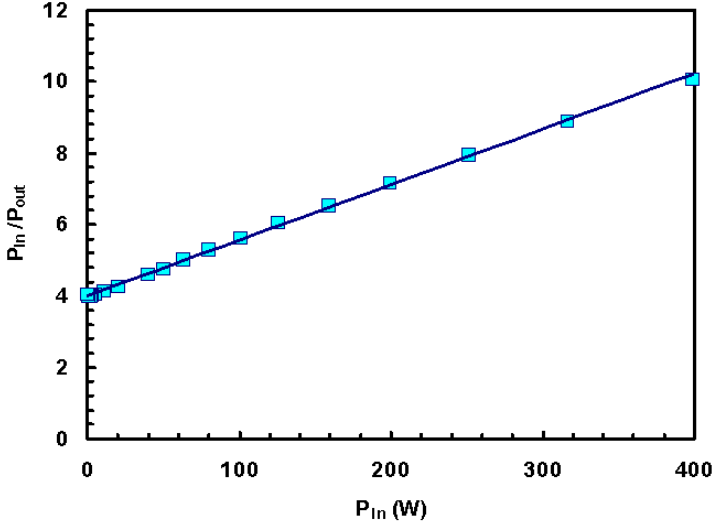
Fig. 24. TPA measurement result. The input power, P_{in}, is not corrected for coupling losses. The linear behavior is maintained up to 400 W

This value of TPA agrees with what has been reported in the literature and with a lorentzian extrapolation of values measured at 1.06 μm [55]. In summary, the value measured for B implies that no practical effect of TPA should be considered in the results of Sect. 3.2.1 for SRS measurements.

3.2.3 Demonstration of Coherent Anti-Stokes Raman Scattering (CARS) in Silicon Waveguides

Coherent Anti-Stokes Raman Scattering (CARS), Parametric Wavelength Conversion (PWC), and Optical Parametric Amplification (OPA) are nonlinear optical processes occurring in fibers and nonlinear crystals [58, 59]. PWC and OPA have been investigated in optical fibers in the context of broadband signal amplification, or as wavelength-conversion mechanisms [60, 61]. The theory that governs these phenomena has been fully developed in Sects. 2.4 and 2.5. The effect involves interaction of three fields: the pump, the Stokes, and the anti-Stokes (a-Stokes) fields, at wavelengths (frequencies) $\lambda_P(\omega_P)$, $\lambda_S(\omega_S)$, $\lambda_{aS}(\omega_{aS})$, respectively. The incoming fields will be the pump, $\boldsymbol{E}_P$ (TE$_0$ mode), and the Stokes, $\boldsymbol{E}_S$ (TM$_0$ mode). In this section, a demonstration of the effect of Stokes to anti-Stokes parametric conversion in silicon waveguides and its counterpart, that is, a-Stokes to Stokes conversion, will be presented. The potential for building a CARS-based, silicon wavelength-converter will be discussed in the following section. The experimental setup used for this series of experiments is similar to the one presented above to measure spontaneous Raman emission and SRS in silicon waveguides (see Figs. 15 and 19). As usual, the pump laser is coupled into the TE$_0$ mode,
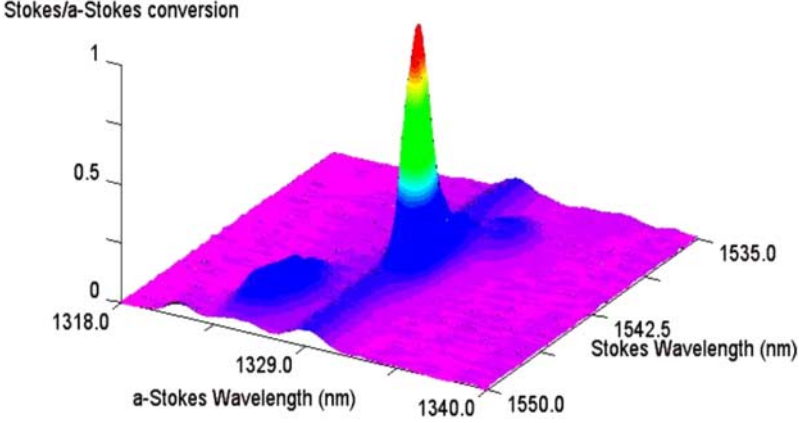
Fig. 25. Plot of the a-Stokes spectra collected for a given value of the signal (Stokes wavelength). The z-axis represents the Stokes/a-Stokes conversion efficiency, normalized to unity. Note the clear appearance of two "satellite" resonances, as mentioned in the text

and the signal laser is coupled into the TM_0 mode. The signal laser in this case consists of two different types. The Stokes signal laser can be scanned in a wavelength range from 1530 nm to 1560 nm, and the anti-Stokes signal laser is fixed at the Raman anti-Stokes wavelength, i.e. 1328.8 nm. Figure 25 shows the a-Stokes spectra measured as a function of the Stokes signal wavelength. The spectra were collected by scanning the spectrum analyzer in the range 1318 nm to 1340 nm, while the Stokes laser was set at a wavelength λ_S, and the pump laser effective power was 0.7 W. The wavelength of the Stokes laser, λ_S, was tuned from 1535 nm to 1550 nm. There is a clear peak at 1328.8 nm of anti-Stokes emission when the Stokes laser is tuned to 1542.3 nm. The latter corresponds to the peak of the spontaneous Raman emission in silicon. The nature of the weaker features in Fig. 25 is due to the wavelength-dependent character of the phase-matching parameter, $\Delta\beta$, in the SOI waveguide, and the characteristic $Sinc^2$ dependence of the conversion efficiency with $\Delta\beta$ (Sect. 2.6).

To obtain the down-conversion efficiency, the a-Stokes integrated power was measured as a function of the Stokes signal power, for different values of pump power. The result is shown in Fig. 26.

From the slopes in Fig. 26, the maximum Stokes/anti-Stokes power conversion efficiency measured for this particular waveguide is found to be $\sim 10^{-6}$ for an effective pump power of ~ 0.7 W. By using the signal laser at 1328.8 nm through the TM_0 port of the PBS, the opposite effect is found, namely, power conversion into Stokes wavelength. Figure 27 shows the effect for different values of the a-Stokes laser power, with the pump laser effective power set at 0.7 W. In this case it was not possible to obtain a plot like the one shown
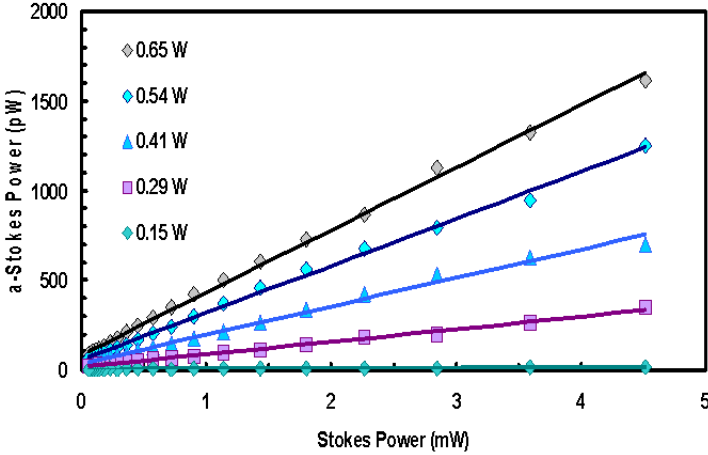
Fig. 26. Stokes to a-Stokes conversion efficiency. The Stokes power was varied using a VOA. The efficiency, defined as the slope of the plots shown, increases with pump power, as expected
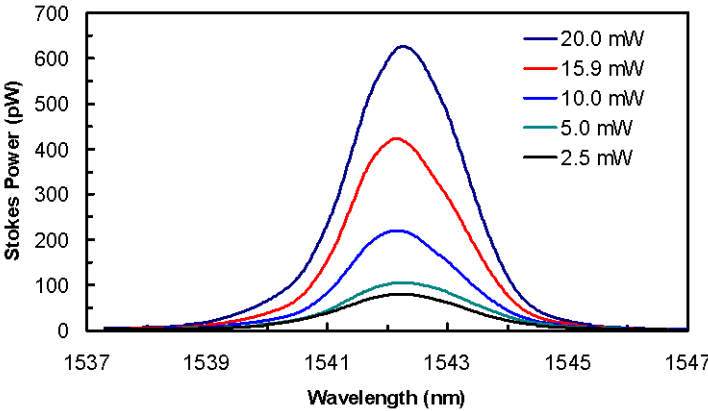

Fig. 27. Anti-Stokes to Stokes conversion. The a-Stokes power was varied using a VOA. Stokes power shown is not corrected for collection efficiency ($\sim 10\,\mathrm{dB}$ from output facet of waveguide)

on Fig. 25 because the a-Stokes laser used is not tunable across such a wide range.

3.3   Demonstration of Parametric Raman Wavelength Conversion in Silicon

The results shown up to this point have demonstrated the potential for light amplification and wavelength conversion in silicon optical circuits. The analysis carried out in Sects. 2.4 and 2.5 led us to the conclusion that the para-
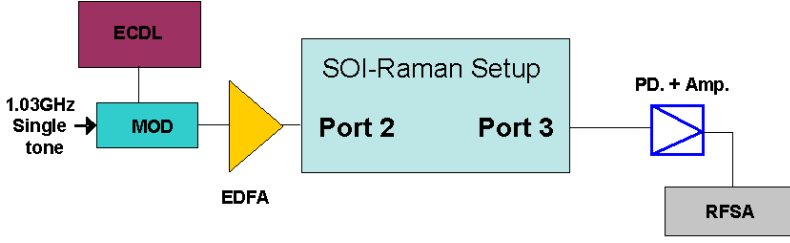
**Fig. 28.** CARS-based, SOI signal transmission switch

metric coupling between pump, Stokes and anti-Stokes waves, through the Raman susceptibility, can be used to transfer information between the wavelength channels. It has been demonstrated that the conversion efficiency of this process is dependent upon the phase difference between the three waves, the intensity of the Pump wave, and the Raman susceptibility of the medium, as detailed in Sect. 2.5. The experimental setup used to realize this wavelength-conversion scheme is shown in Fig. 28. The SOI-Raman setup consists of the same pump laser and waveguide as described in the previous experiments. An external cavity diode laser (ECDL) is used as the Stokes source at 1542 nm. The ECDL is externally modulated and amplified by an Erbium-doped fiber amplifier (EDFA), in order to maximize the amount of down-converted, a-Stokes signal. At the output, a BPF filter is used to extract the converted a-Stokes signal, at 1328.5 nm, before photodetection and 40 dB electrical amplification.

Figure 29a shows the converted a-Stokes signal spectrum. Note that the FWHM for wavelength conversion, which is approximately 250 GHz, is determined solely by the pump laser linewidth. Figure 29b shows the conversion of 1.03 GHz RF modulation from 1542 nm to 1328.5 nm. The input RF signal power applied to the Stokes wavelength is shown in the inset. The measured electrical Signal to Noise Ratio (SNR) is 34 dB. Figure 30a shows the wavelength-converted eye diagram when a 1 Mb/s PRBS $(2^7 - 1)$ modulation is applied to the Stokes laser. Figure 30b depicts the measured electrical SNR versus the input Stokes optical power, along with the theoretical fit. Also shown in Fig. 30b is the SNR when the conversion efficiency is increased by 10 dB.

As has been discussed in Sect. 2.7, by proper rib waveguide design, the waveguide birefringence term can be used to obtain phase matching conditions. This hypothesis has been verified using numerical simulations [30]. Under these conditions, with 0.7 W of pump power coupled into a waveguide with 1 μm^2 single-mode cross-section, the conversion efficiency would be approximately 65%. As also mentioned in Sect. 2.7, if the proper design is used for the SOI waveguide, a polarization-insensitive device can be envisioned. This would double the effective data-processing capacity of the device, by using polarization multiplexing.
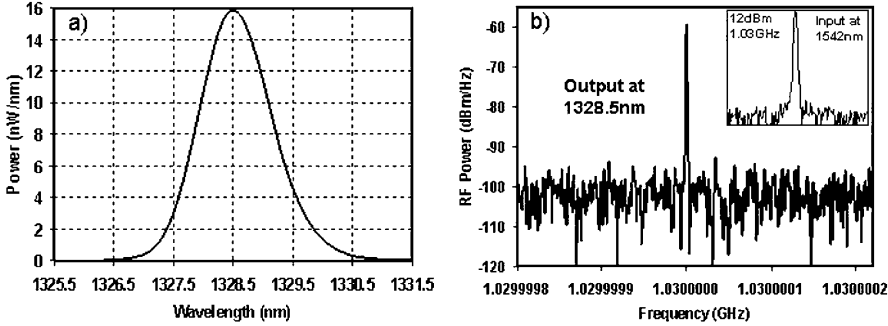
Fig. 29. (a) Maximum a-Stokes signal obtained. (b) Single-tone data conversion at 1.03 GHz. The *inset* shows the incoming signal at 1542.3 nm
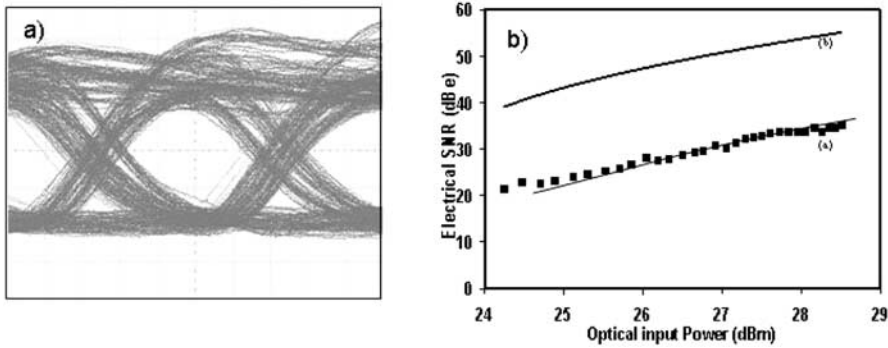
Fig. 30. Wavelength Conversion: (*left*) Eye diagram (1 Mb/s), (*right*) Electrical SNR: Measured (*squares*) and calculated (*solid lines*)

4 Summary

This chapter has outlined a method for light generation, amplification and wavelength conversion in silicon using stimulated Raman processes. These effects are routinely observed in optical fiber; however, several kilometers of length are required to do so. What enable us to achieve these processes on millimeter length scales on a chip are two fundamental differences between an optical fiber and a silicon microstructure. The first is the difference in atomic structures. An amorphous material such as the silica fiber supports many vibrational modes, hence the Raman gain has a very large bandwidth and a low peak value, requiring long interaction lengths for the effect to be observed. In contrast, silicon is single crystal and supports only three optical vibration modes. The result is a much narrower gain bandwidth but a much higher gain peak (nearly 10^4 times higher). Second, is the difference in modal areas. The large index-contrast in the silicon/SiO_2 waveguides results in a mode area that is approximately 100 times smaller (assuming $0.8\,\mu m^2$ waveguides) than in a standard single mode fiber (mode area $= 80\,\mu m^2$).

The proportionally higher power density in the silicon waveguide lowers the threshold for nonlinear optical processes.

The intrinsic Raman bandwidth in silicon is 105 GHz, and it is broadened in the experiments by the pump laser linewidth (typically $\sim 2\,\mathrm{nm}$). The resulting bandwidth is sufficient for amplifying several WDM channels. The bandwidth can be broadened by broadening the pump linewidth even further (although this reduces the peak gain) or by using multiple pump wavelengths.

The Raman phenomenon is fully tunable; the tuning range is only limited by the available pump wavelengths. This is an advantage over the nanocrystal approach for light generation and amplification. In addition, the Raman effect can also perform wavelength conversion, a critical function needed for optical packet switching. Wavelength conversion in silicon is yet to be demonstrated with other techniques. Another important advantage of this approach is that it does not require rare-earth dopants or nanostructures. Hence, it is truly compatible with silicon IC manufacturing.

Going forward, low loss waveguides with small cross sections are required for realizing high performance devices. Surface roughness produces strong scattering and high propagation loss due to the high index contrast between the silicon waveguide core and the cladding (air or SiO_2). As such, losses of silicon waveguides tend to increase with reduction in cross section [62]. Fortunately, new waveguide fabrication processes that are in development promise low-loss waveguides with submicron cross sections [63]. Naturally, one must be able to efficiently couple light into these structures. Several novel approaches for high efficiency coupling into submicron waveguides with impressive results have been recently demonstrated [64].

References

1. B. Jalali, S. Yegnanarayanan, T. Yoon, T. Yoshimoto, I. Rendina, F. Coppinger: Advances in Silicon-on-Insulator Optoelectronics, IEEE J. of Sel. Top. in Quant. El. **4**, 938–947 (1998)
2. L. Pavesi, L. Dal Negro, C. Mazzoleni, G. Franzo, F. Priolo: Optical gain in silicon nanocrystals, Nature **408**, 440 (2000)
3. M. H. Nayfeh, N. Barry, J. Therrien, O. Akcakir, E. Gratton, G. Belomoin: Stimulated blue emission in reconstituted films of ultrasmall silicon nanoparticles, Appl. Phys. Lett. **78**, 1131 (2001)
4. P. M. Fauchet, J. Ruan: Towards the first silicon laser, NATO Series (Kluwer, New York 2003), p. 197
5. L. Khriachtcheve, M. Rasanen, S. Novikov, J. Sinkkonen: Optical gain in Si/SiO_2 lattice: Experimental evidence with nanosecond pulses, Appl. Phys. Lett. **79**, 1249 (2001)
6. K. Luterova, I. Pelant, I. Mikulskas, R. Tomasiunaset, D. Muller, J. J. Grob, J. L. Rehspringer, B. Honerlage: Stimulated emission in blue-emitting Si^+-implanted SiO_2 films, J. Appl. Phys. **91**, 2896 (2002)
7. M. Ivanda, U. V. Densica, C. W. White, W. Kiefer: Towards the first silicon laser, NATO Series (Kluwer, New York 2003), p. 191

8. L. Dal Negro, M. Gazzanelli, N. Daldosso, Z. Gaburro, L. Pavesi, F. Priolo, D.Pacifici, G. Franzo, F. Iacona: Stimulated emission in plasma-enhanced chemical vapour deposited silicon nanocrystals, Physica E **16**, 297 (2003)

9. L. Pavesi: Will silicon be the photonic material of the third millenium?, J. Phys. Condens. Matter **15**, R1169–R1196 (2003)

10. S. Coffa, G. Franzo, F. Priolo: High efficiency and fast modulation of Er-doped light emitting Si diodes, Appl. Phys. Lett. **69**, 2077 (1996)

11. S. Coffa, G. Franzo, F. Priolo, A. Pacelli, A. Lacaita: Direct evidence of impact excitation and spatial profiling of excited Er in light emitting Si diodes, Appl. Phys. Lett. **73** 93 (1998)

12. M. E.Castagna: Quantum Dot Materials and Devices for Light Emission in Silicon, Proc. 32th European Solid-State Device Res. Conf., Firenze, Italy, (University of Bologna 2002) p. 439–442

13. S. Coffa: ST sets world record for silicon light emission, ST Press Release, **3** (2002)

14. M. A. Green, J. Zhao, A. Wang, P. J. Reece, M. Gal: Efficient Silicon Light-emitting diodes, Nature **412**, 805 (2001)

15. R. A. Soref: Thin Solid Films **294**, 325 (1997)

16. G. Dehlinger, L. Diehl, U. Gennser, H. Sigg, J. Faist, K. Ensslin, D. Grutzmacher: Intersubband electroluminescence from silicon-based quantum cascade structures, Science **290**, 2277 (2000)

17. L. Diehl, D. Mentese, H. Sigg, E. Muller, D. Grutzmacher, U. Gennser, I. Sagnes, T. Fromhertz, J. Stangl, T. Roch, G. Bauer, Y. Campidelli, O. Kermarrec, D. Bensahel, J. Faist: Electroluminescence from strain-compensated $Si_{0.2}Ge_{0.8}$/Si quantum-cascade structures based on a bound-to-continuum transition, Appl. Phys. Lett. **81**, 4700 (2002)

18. S. A. Lynch, R. Bates, D. J. Paul, D. J. Norris, A. G. Cullis, Z. Ikonic, R. W. Kelsall, P. Harrison, D. D. Arnone, C. R. Pidgeon: Intersubband electroluminescence from Si/SiGe cascade emitters at terahertz frequencies, Appl. Phys. Lett. **81**, 1543–1545 (2002)

19. J. Faist, F. Capasso, D. L. Sivco, C. Sirtori, A. L. Hutchinson, A. Y. Cho: Quantum cascade laser, Science **264**, 553 (1994)

20. R. Claps, D. Dimitropoulos, B. Jalali: Stimulated raman scattering in silicon waveguides, IEE Electron. Lett. **38**, 1352–1354 (2002)

21. R. Claps, D. Dimitropoulos, Y. Han, B. Jalali: Observation of Raman emission in silicon waveguides at 1.54 µm, Opt. Express **10**, 1305–1313 (2002)

22. D. Dimitroupoulos, R. Claps, B. Jalali: Prospects for Raman amplification in silicon, Materials Research Society, MRS Annual Meeting (Boston, MA 2002)

23. D. Dimitropoulos, R. Claps, B. Jalali: Nonlinear optics in silicon waveguides: stimulated Raman scattering and two-photon absorption, Proc. SPIE **4987** (2003), pp. 140–148

24. R. Claps, V. Raghunathan, D. Dimitropoulos, B. Jalali: Raman emission in Silicon waveguides: Prospect for Silicon amplifier and Laser (CLEO, Baltimore, MD 2003)

25. R. Claps, D. Dimitropoulos, V. Raghunathan, Y. Han, B. Jalali: Observation of stimulated Raman scattering in Silicon waveguides, Opt. Express **11**, 1731–1739 (2003)

26. B. Jalali, R. Claps, D. Dimitropoulos: Integrated Photonic Research (IPR) (Washington, DC 2003)

27. D. Dimitropoulos, B. Houshmand, R. Claps, B. Jalali: Coupled-mode theory of Raman effect in silicon-on-insulator waveguides, Opt. Lett. **28** (2003)
28. R. Claps, V. Raghunathan, D. Dimitroupoulos, B. Jalali: Anti-stokes Raman conversion in silicon waveguides, Opt. Express **11**, 2862–2872 (2003)
29. V. Raghunathan, R. Claps, D. Dimitropoulos, B. Jalali: Wavelength Conversion in Silicon Waveguides using Parametric Stokes to Anti-Stokes Coupling (CLEO 2004), submitted
30. D. Dimitropoulos, V. Raghunathan, R. Claps: Silicon Optical Wavelength conversion based on Parametric Raman effect in Dispersion compensated waveguides, manuscript in preparation
31. D. Dimitropoulos, V. Raghunathan, R. Claps, B. Jalali: Phase-matching for Efficient Parametric Wavelength Conversion in Silicon Waveguides, Opt. Express (submitted)
32. P. A. Temple, C. E. Hathaway: Multiphonon Raman Spectrum of Silicon, Phys. Rev. A **7**, 3685 (1973)
33. M. Cardona, G. Guntherodt: *Light Scattering in Solids II*, Top. Appl. Phys. **50** (Springer, Berlin 1982)
34. A. Yariv: *Quantum Electronics*, 3rd edn. (Wiley, New York 1988)
35. J. M. Ralston, R. K. Chang: Spontaneous-Raman-scattering efficiency and stimulated scattering in silicon, Phys. Rev. B **2**, 1858–1862 (1970)
36. R. H. Stolen, E. P. Ippen: Raman gain in glass optical waveguides, Appl. Phys. Lett. **22**, 276–278 (1973)
37. R. H. Stolen: Nonlinear properties of optical fibers, in *Optical Fiber Telecommunications* (Academic Press, New York 1979)
38. D. H. Choi, W. J. R. Hoefer: The Finite-Difference Time-Domain method and its applications to Eigenvalue problems, IEEE Trans. Microwave Theory Tech. (1986), pp. 1464–1470
39. R. Loudon, *The Quantum Theory of Light*, 3rd edn. (Oxford University Press)
40. G. P. Agrawal: *Non Linear Fiber Optics* (Academic Press, San Diego 2001)
41. Y. R. Shen, N. Bloembergen: Theory of stimulated Brillouin and Raman scattering, Phys. Rev. **137**, A1787–A1805 (1965)
42. E. Golovchenko, P. V. Mamyshev, A. N. Pilipetskii, E. M. Dianov: Mutual influence of the parametric effects and stimulated Raman scattering in optical fibers, IEEE. J. Quant. Elec. **26**, 1815–1820 (1990)
43. R. W. Boyd: *Nonlinear Optics* (Academic Press, San Diego 1992)
44. H. H. Li: Refractive index of silicon and germanium and its wavelength and temperature derivatives, J. Phys. Chem. Ref. Data **9**, 591–658 (1980)
45. T. Saito, K. Suto, J. Nishizawa, M. Kawasaki: Spontaneous Raman scattering in [100], [110] and [11-2] directional GaP waveguides, J. Appl. Phys. **90**, 1831 (2001)
46. R. G. Smith: Optical power handling capacity of low loss optical fibers as determined by stimulated Raman and Brillouin scattering, Appl. Opt. **68**, 2489 (1972)
47. S. V. Rao, K. Moutzouris, M. Ebrahimzadeh, A. De Rossi, G. Dintz, M. Calligaro, V. Ortiz, V. Berger: Influence of scattering and two-photon absorption on the optical loss in GaAs-Al_2O_3 nonlinear waveguides measured using femtosecond pulses, IEEE J. Quant. Elec. **39**, 478–486 (2003)
48. Spectra-Physics Telecom: Model RL5 Raman Fiber Laser Specifications
49. M. Grimsditch, M. Cardona: Absolute cross-section for Raman scattering by phonons in silicon, Phys. Stat. Sol. B **102**, 155 (1980)

50. H. K. Tsang, C. S. Wong, T. K. Lang, I. E. Day, S. W. Roberts, A. Harpin, J. Drake, M. Asghari: Optical dispersion, two-photon absorption and self-phase modulation in silicon waveguides at $1.5\,\mu\mathrm{m}$ wavelength, Appl. Phys. Lett. **80**, 416 (2002)
51. C. Xu, W. Denk: Two-photon optical beam induced current imaging through the backside of integrated circuits, Appl. Phys. Lett. **71**, 2578 (1997)
52. K. Kikuchi: Optical sampling system at $1.5\,\mu\mathrm{m}$ using two photon absorption in Si avalanche photodiode, IEE Elecron. Lett. **34**, 1354 (1998)
53. T. K. Liang, H. K. Tsang, I. E. Day, J. Drake, A. P. Knights, M. Asghari et al.Silicon waveguide two-photon absorption detector at $1.54\,\mu\mathrm{m}$ wavelength for autocorrelation measurements, Appl. Phys. Lett. **81**, 1323 (2002)
54. J. M. Ralston, R. K. Chang: Optical limiting in Semiconductors, Appl. Phys. Lett. **15**, 164 (1969)
55. J. F. Reintjes, J. C. McGroddy: Indirect two-photon transitions in Si at $1.06\,\mu\mathrm{m}$, Phys. Rev. Lett. **30**, 901 (1973)
56. M. Dinu, F. Quochi, H. Garcia: Third-order nonlinearities in silicon at telecom wavelengths, Appl. Phys. Lett. **82**, 2954 (2003)
57. M. Sheik-Bahae, E. W. Stryland: *Optical Nonlinearities in the Transparency Region of Bulk Semiconductors, Nonlinear Optics in Semiconductors I*, Semicond. Semimet. **58** (Academic Press, 1999)
58. H. Vogt: Coherent and hyper-Raman techniques, in M. Cardona, G. Guntherodt (Eds.): *Light Scattering in Solids II*, Top. Appl. Phys. **50** (Springer, Berlin 1982), chap. 4
59. M. C. Ho, K. Uesaka, M. Marhic, Y. Akasaka, L. G. Kazovsky: 200-nm-bandwidth fiber optical amplifier combining parametric and Raman gain, J. Light. Technol. **19**, 977 (2001)
60. M. E. Marhic, K. K.-Y. Wong, L. G. Kazovsky: Prospects for CW Fiber OPAs and OPOs, CLEO 2003, Baltimore, MD, USA, paper no. CTuA1 (2003)
61. J. K. Chee, J.-M. Liu: Polarization-dependent parametric and Raman processes in a birefringent optical Fiber, IEEE J. Quant. Elec. **26**, 541 (1990)
62. T. Zinke et al.: Comparison of optical waveguide losses in silicon-on-insulator, IEE Elec. Lett. **29**, 2031 (1993)
63. P. Koonath, K. Kishima, T. Indukuri, B. Jalali: SIMOX sculpting of 3-D nano-optical structures, LEOS Annual Meeting (Tucson, AZ, USA 2003)
64. IEEE LEOS Summer Topical Meetings, 14–16 July 2003, Vancouver, BC, Canada, Proceedings Session TuA2: Coupling Issues in Microphotonics, IEEE Catalog Number 03TH8701

Index